AIMS Energy

AIMS Energy, 14(3): 571–601.
DOI: 10.3934/energy.2026024
Received: 23 February 2026
Revised: 29 April 2026
Accepted: 07 May 2026
Published: 26 May 2026

https://www.aimspress.com/journal/energy

Research article

Deep learning prediction and optimization of biomass-powered organic Rankine cycle

Moses O. Petinrin[1,2,*], Eniola D. Otolorin[1], Olumide A. Towoju[3] and Patrick M. Singh[2,4]

[1] Department of Mechanical Engineering, University of Ibadan, Ibadan, Nigeria
[2] School of Mechanical Engineering, Fiji National University, Suva, Fiji
[3] Department of Mechanical Engineering, Lead City University, Ibadan, Nigeria
[4] School of Information Technology, Engineering, Mathematics and Physics, The University of the South Pacific, Suva, Fiji

* **Correspondence:** Email: layopet01@yahoo.com, mo.petinrin@ui.edu.ng; Tel: +2348035148170.

Abstract: Increasing demand for sustainable energy is driving significant interest in biomass-powered ORC systems, especially for small-scale, off-grid power generation. However, due to the nonlinear coupling between the operating parameters, it remains difficult to predict many different performance indicators, or rank performance to identify the best system configurations. This study seeks to address these issues by developing a deep neural networks (DNN) model with thermodynamic simulation, multi-objective optimization, and decision analysis to predict biomass organic Rankine cycle (ORC) performance, with the aim of optimizing performance. Data was generated in matrix laboratory (MATLAB) using CoolProp based on two biomass fuels, coconut shell and cornstalk, and operating ranges that included pressures of 2.6–3.5 MPa, and lower cycle temperature of 300.15–310.15 K for R245fa as working fluid. The nine decision variables included mixture strength, biomass flowrate, and component efficiencies. The DNN predicted four exergy-based outputs: net power, cycle efficiency, exergy efficiency of heat transfer fluid–organic Rankine cycle (HTF–ORC) circuits, and the overall exergy efficiency of the biomass plant. Pareto-based optimization, was implemented using particle swarm optimization (PSO), which produced non-dominated solutions from which the optimal decision variables were identified based on technique for order preference by similarity to ideal solution (TOPSIS) method. The results indicated coconut shell performance was greater than that for cornstalk, with optimal net power ranging from 1350–1460 kW, cycle efficiency values around 18.4%, HTF–ORC exergy efficiency values between 26–27%, and plant exergy efficiency between 6.5–6.9%. The most efficient points correlated with the highest operating temperatures and pressures. The mixture strength and biomass mass flowrate showed proportional increases to power targets, reaffirming the validity of the thermodynamic analysis and optimization. The DNN-PSO-TOPSIS approach appropriately captures the multi-parametric interactions that govern ORC performance, providing a powerful and scalable framework for the design of efficient biomass-to-power systems for renewable energy uses.

Keywords: biomass; deep learning; exergy efficiency; organic Rankine cycle; particle swarm optimization

1. Introduction

Renewable energy applications have drawn attention from around the world for a number of reasons, such as the development of renewable energy technology, the reduction of fossil fuel consumption, sustainable development, and energy security. Non-renewable energy sources such as fossil fuels have been used excessively, and their emissions have been increasingly causing harmful environmental problems, including climate change and global warming. In recent decades, the emission of greenhouse gases has increased exponentially, with their attendant ecological impacts [1,2]. Approximately 21.3 billion tons of carbon dioxide (CO_2) and other greenhouse gases (GHG) are produced annually as a result of burning fossil fuels. According to reports, just half of that quantity can be eliminated by natural processes. As a result, the atmosphere's CO_2 content increases by 10.65 billion tons per year [3]. Many countries under the Paris Agreement are committed to supporting the global effort to reach net-zero emissions targets by 2050 as a result of climate change. Renewable energy sources, which are essential for de-carbonizing the global economy and reducing the impact of climate change, are being accelerated to reduce the consumption of fossil fuels [4,5].

Thus, research into environmentally friendly, sustainable, and renewable energy sources is crucial. Thus, to continue satisfying increasing global demand, which rises at exponential levels, while trying to reduce the impact of climate change, renewable energy technologies such as wind, solar, biomass, hydro, geothermal, and hydrogen technologies have gained significant popularity in the 21st century [1,6,7]. The shift to renewable energy is motivated by the need to combat climate change, decrease greenhouse gas emissions, and provide energy security. Renewable energy sources and cycles that employ thermal energy at low temperatures and thermal losses have been warmly received in light of recent concerns about energy conservation and reducing greenhouse gas emissions brought on by the use of fossil fuels [8].

Biomass is an organic and biodegradable energy source from plants, animals, and living things. Usually, it is made up of cellulose, hemicelluloses, lignin, and extractives such as ash, lipids, and resins [9]. Because biomass is a renewable energy source with fuel cycles devoid of net greenhouse gas emissions, it is regarded as a sustainable and carbon-neutral energy source [9,10]. Biomass is derived from a variety of sources, such as forests, agricultural and forestry wastes, human and animal wastes, and energy crops. Due to its global accessibility, including remote locations without grid connectivity, biomass-based power generation supports rural communities by creating jobs and socioeconomic advantages. Direct combustion, biochemical processes, agrochemical processes, and thermochemical processes (pyrolysis, gasification, or torrefaction) are the four main categories of conversion technologies for the use of biomass energy. However, direct combustion and gasification are the most widely employed processes for converting biomass energy into electrical power [5,11].

The fact that biomass has a lower energy density than fossil fuels is a major drawback for this energy source. This limitation has prompted the need to explore alternative methods of fully exploiting its potential in electricity production. This has led to the development of processes, such as densification (pelletizing and briquetting), carbonization, and gasification, that can improve biomass handling and combustion characteristics and help convert biomass into an energy-dense form. These processes have also enabled better integration of biomass into energy systems that exploit low-grade heat of combustion, such as the Brayton cycle, Kalina cycle, and organic Rankine cycle (ORC) [7,11,12]. The ORC has been of particular interest and gained acceptance relative to many of the cycles discussed in the literature, due to its versatile operational conditions, high safety levels, low maintenance requirements, and relatively efficient thermal performance [4,12,13]. The ORC is more efficient at capturing low-temperature energies, such as biomass, geothermal, solar thermal, and industrial waste heat, compared with the many existing technologies available [8,14,15].

An ORC cycle is a Rankine cycle, like a conventional steam power plant, that has the working fluid or working medium as an organic substance, usually hydrocarbons or synthesized refrigerants. There has been a great deal of interest in this technology for the past few years due to the many possibilities of its applications [15]. According to reports, ORC researchers have classified the systems in multiple ways, but most typically they are classified into three systems: small-scale systems (0.5–10 kW) for homes, small businesses, or schools, especially in off-grid regions with reliable biomass; medium-scale systems (up to 1 MW) for rural areas or agricultural facilities; and large-scale systems (up to 10 MW) for industrial uses or rural electricity provision [7].

The temperature of the heat source is a critical parameter for selecting a suitable working fluid for the ORC plant. Many organic working fluids like R245fa, R245ca, R134a, R113, R123, R1234yf, R1224yd(Z), R1233zd(E), ethanol, isobutane (R600a), butane (R600), pentane (R601), isopentane (R601a), and HFOs (hydrofluoroolefins) have been studied and used in ORC power plants [7,16–19]. Due to their thermodynamic properties including zero ozone depletion potential, low global warming potential, thermal stability in addition to low boiling point, critical pressure, non-corrosive, non-toxic, and compatibility with fluid systems operating conditions, these fluids are selected to provide flexibility for a variety of applications in ORC systems [14,16,20,21].

In general, the design of ORC systems encompasses the following considerations: selection and sizing of components, optimization of operating parameters, selection of cycle configuration, and working fluids. Thus, the objective of an optimal ORC is to effectively convert the heat source energy [22]. Many of the previous studies adopted the traditional methods of using isolated studies and/or thermodynamic modeling, which yields precisely correct results, but which are plagued with substantial convergence problems that make the resolution of more complicated problems or multiple thermal engines challenging [23]. Moreover, ORC plants are extremely complicated to optimize through traditional nonlinear optimization techniques for the very reason that there are a substantial number of mathematical models, and one must consider those variables [24]. The recent surge of advancements of artificial intelligence (AI) created even more options to predict and optimize the design and performance of ORC systems, which simplifies the very complicated process [25]. By utilizing this technology, it is possible to solve very challenging and intricate ORC system designs and optimization to support a more efficient and sustainable energy future. In recent times, the machine learning subfield of AI has increasingly been employed as a viable tool for predicting and analyzing energy systems [26,27].

Furthermore, deep learning has become a very powerful machine learning technique. Specifically, deep learning takes advantage of artificial neural networks to process large datasets while performing complex calculations. Essentially, deep learning is machine learning that replicates the design and function of the human brain [28–30]. Common architectures used in various domains of deep learning include deep neural networks (DNNs), convolutional neural networks (CNNs), Transformer architectures, recurrent neural networks (RNNs), long short-term memory networks (LSTMs), graph neural networks, variational autoencoders (VAE), deep Q-networks (DQN), deep belief networks (DBN), and generative adversarial networks (GAN) [25]. Mert et al. [29] used stepwise multilinear regression and deep learning to estimate the behavior of a 10 kW ORC system on a number of operating parameters of the system. They later proposed an interoperability framework based on the developed method. Flores-Tlacuahuac et al. [31] predicted the thermal and exergy efficiencies from a set of noisy measurements with deep learning nonlinear mappings to raise the energy recovery from waste-energy sources for ORC systems. Kim et al. [32] developed a deep learning algorithm with two hidden layers from experimental data to predict the performance of a radial flow turbine in ORC. Their results indicated a prediction that accurately captured the noisy measurements recorded from the experiment. Daniarta et al. [28] applied the DNN approach to predict the isentropic efficiency of a multi-vane expander of an ORC system under varying operating parameters. They established a performance mapping with the DNN to demonstrate its effectiveness in accurately predicting the isentropic efficiency.

Modeling of biomass-based ORC systems has advanced significantly, but predicting multiple performance metrics at once, such as net power production, thermal efficiency, exergy loss, and exergy efficiency, has remained a challenge. Due to their theoretical or empirical foundations, the majority of current models are unable to take into consideration the intricate and nonlinear relationships between various input parameters, such as biomass type, flow rate, cycle temperatures, and desired outputs. There are limited studies that examine combined multiple output prediction in biomass ORC systems, despite the fact that machine learning techniques, such as deep learning, have been applied for the prediction of single performance parameters in a number of studies. In system optimization, where a comprehensive understanding of all relevant performance parameters is crucial for making the right decisions that will result in modifications that improve efficiency and sustainable design, such an information gap is particularly significant. Furthermore, there is a void in the literature for state-of-the-art prediction models that can take into consideration this multifactorial nature because the studies that are now accessible are not made to multi-objectively evaluate the impact of input features on all key performance outputs simultaneously.

A DNN model is used in this study to predict several outputs for biomass-powered ORC systems, including net power output, cycle efficiency, exergy efficiency of the heat transfer fluid–organic Rankine cycle (HTF–ORC), and exergy efficiency of the biomass plant, in an effort to address the identified gap. The dataset to be used will be generated from the theoretical analysis of the biomass ORC system using MATLAB and CoolProp with ten input features: the type of biomass, mixture strength, mass flowrate of biomass, combustion efficiency, turbine inlet temperature, lower cycle temperature, upper cycle pressure, mass flowrate of working fluid, pump efficiency, and turbine efficiency. Following this approach, the study aims to create an accurate and scalable model that evaluates the complex interdependencies between input features and system performance. The DNN model is further enhanced using particle swarm optimization (PSO) to provide the Pareto front, and the multi-objective decision-making method, the technique for order preference by similarity to ideal solution (TOPSIS), was additionally employed. The aim is to optimize the predictive capability of the model at different operating conditions, support the optimization of biomass-ORC toward efficiency and sustainability in practice, and offer guidance for their implementation and usage.

2. Methodology

This section outlines the methodology for predicting the performance of biomass-powered ORC systems including net power output, cycle efficiency, the exergy efficiency of the HTF–ORC, and the exergy efficiency of the biomass plant. Our methodology consists of data collection and preparation, the development of a deep learning model to provide solutions to the problem, and creating an evaluation process and methodology. The research employs a thermodynamic analysis of the biomass-powered ORC cycle with R245fa as the working fluid, data generation using MATLAB and CoolProp, deep learning-based prediction, and multi-objective optimization using PSO and TOPSIS. The workflow outlines the exact methodology for biomass characterization, combustion analysis, thermodynamic modeling, data preparation, DNN training, with performance evaluation and optimization.

2.1. Biomass selection and combustion analysis

Two sources of dry biomass feedstock, coconut shell and cornstalk, were chosen to be the primary solid fuels and biomass for the biomass-powered ORC. These are also common sources of renewable energy in agricultural areas because of their availability and abundance. The ultimate analysis is generally performed in the characterization of biomass to understand the elemental composition for estimating higher heating value (HHV) and lower heating value (LHV). However, for this study, these values were estimated from the elemental compositions from literature [33,34]. This is important because the energy content of the biomass is directly related to the power output of the ORC. The chemical compositions of coconut shell and cornstalk are presented in Table 1. This shows the percentages of the elements carbon (C), hydrogen (H), oxygen (O), nitrogen (N), and sulphur (S), which were applied to calculate the HHV and LHV of the biomass sources based on standard empirical equations. The higher and heating values (kJ/kg) were determined from [35]:

$$HHV = 349.1C + 1178.3H + 100.5S - 103.4O - 15.1N - 21.1 \times c_A \tag{1}$$

The LHVs (kJ/kg) were then estimated from the HHVs by reducing the heat released from the moisture content and hydrogen combustion using Eq (2):

$$LHV = HHV \times 0.01 \times \left(100 - c_M - c_A\right) - 24.42\left(c_M + 0.09H\left(100 - c_M - c_A\right)\right) \tag{2}$$

Table 1. The chemical compositions of selected biomass sources [33,34].

Biomass feedstock	C (%wt)	H (%wt)	N (%wt)	S (%wt)	O (%wt)	Ash (c_A) (%wt)
Coconut shell	50.34	6.26	0.00	0.31	42.08	1.02
Cornstalk	42.02	5.58	1.24	0.43	43.53	7.19

From Eqs (1) and (2), c_A is the ash content of the non-combustible mineral after combustion, and c_M represents the moisture content of the biomass. However, it is assumed in this study that the biomass is perfectly dried with no moisture content.

The combustion analysis was performed after determining the HHVs and LHVs to estimate the flue heat content and temperature for the ORC system based on the thermodynamic properties of the combustion process for ranges of mixture strength, mass rate of biomass addition, and combustion efficiency. The general equation for the combustion process, assuming a complete combustion in the presence of excess oxygen, is written as [36]

$$C_aH_bO_cN_dS_e + x\left(O_2 + 3.76N_2\right) \rightarrow aCO_2 + \frac{b}{2}H_2O + eSO_2 + \left(\frac{d}{2} + 3.76x\right)N_2$$
$$+\left[x - \left(a + \frac{b}{4} + e - \frac{c}{2}\right)\right]O_2 \tag{3}$$

The mixture strength, which is a measure of the degree of completeness of the combustion process, is the ratio of theoretical to actual air for a given unit mass of fuel. It is the quality of richness (greater than 100%) or leanness (less than 100%) of the mixture of air and fuel. That is

$$\lambda = \frac{AFR_{stoic}}{AFR_{actual}} \times 100 \tag{4}$$

where AFR is the ratio of mass of air to the mass of biomass fuel.

By equating the heat release by combustion, which is equivalent to the LHV, to the sensible enthalpy rise of the combustion products, the adiabatic flame temperature (AFT), which represents the maximum temperature attainable by combustion products, is calculated from

$$T_{AFT} = T_0 + \frac{LHV}{\sum_i n_i c_{p,i}} \tag{5}$$

where T_0 is the reference temperature at 298.15 K, n_i is the number of moles of a combustion product formed per mass of fuel ($\text{kmol}_i/\text{kg}_{\text{fuel}}$), and $c_{p,i}$ is the molar specific heat capacity of a product in $\text{kJ/kmol}_i\text{.K}$, which is estimated from stoichiometric combustion analysis of biomass.

The combustion efficiency, η_c of 85%, is factored in to consider the influence of system design and operations, fuel quality, mixing and swirling of air and biomass, combustion temperature and pressure, heat loss and recovery, volatile matter, and residence time, among others. Thus, the heat of combustion determined from the stoichiometric combustion analysis of biomass is

$$\dot{Q}_c = \eta_c \dot{m}_{fuel} LHV \tag{6}$$

and the corresponding flue gas temperature from combustion was evaluated from

$$T_{fg} = T_0 + \frac{\dot{Q}_c}{\dot{m}_{fg} c_{p,fg}} \tag{7}$$

thus, the mass flow rate of flue gas (kg/s) and the weighted specific heat capacity ($\text{kJ/kg}_{\text{fg}}\text{.k}$) of the flue gas are determined, respectively, as

$$\dot{m}_{fg} = \dot{m}_{fuel}\left(1 - c_A + AFR_{actual}\right) \tag{8}$$

and

$$c_{p,fg} = \frac{\sum_i n_i c_{p,i}}{\sum_i m_i} \tag{9}$$

where m_i represents the mass of a combustion product in flue gas per mass of fuel (kg_i/kg_{fuel}).

However, the flue gas temperature at the heat exchanger inlet with HTF was assumed to be approximately 427 °C. This assumption could account for reductions from boiler wall and piping losses, radiation, and possible heat tapping for auxiliary purposes. Also, in practice, this ensures a feasible heat exchanger design and the safe operation of the thermal oil from thermal degradation. While the HTF helps the systems stability in ensuring continuous supply of heat to keep the working fluid from disintegration over time, its thermal range must also be kept in certain range [37,38]. Therefore, the useful thermal energy received by the HTF from the flue gas was obtained from

$$\dot{Q}_{HTF} = \dot{m}_{HTF} c_{p,HTF} \left(T_{HTF,e} - T_{HTF,i} \right) = \dot{m}_{fg} c_{p,fg} \left(T_{fg,i} - T_{fg,e} \right) \tag{10}$$

2.2. Thermodynamic analysis of the ORC system

The thermodynamic analysis of the ORC system was performed in MATLAB using the CoolProp database of thermodynamic properties of fluids. The working fluid selected for this study is R245fa, which is most commonly used in low-temperature ORCs as its thermodynamic properties are more favorable for such applications. The R245fa has been the most frequently used fluid in numerous ORC studies due to its higher thermal stability, efficiency, and relative environmental friendliness when compared to other organic refrigerants [32]. Its properties include a boiling point of 288.05 K, a critical temperature of 427.2 K, a critical pressure of 3.651 MPa, an ODP of 0, a GWP of 1030, and an ASHRAE 34 safety classification of B1 with a flammability class of 1 [17,20,32]. The analysis was based on a closed-loop Rankine cycle in which the flue gas heat input is transformed through the means of the HTF into work by the turbine and heat rejection takes place through the condenser, as depicted in the schematic and *T-s* diagrams of the ORC system shown in Figures 1 and 2, respectively.

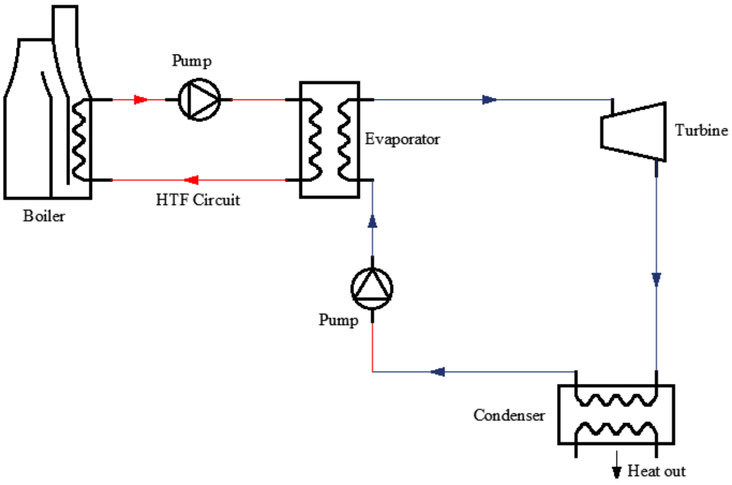

Figure 1. The schematic of the ORC system.

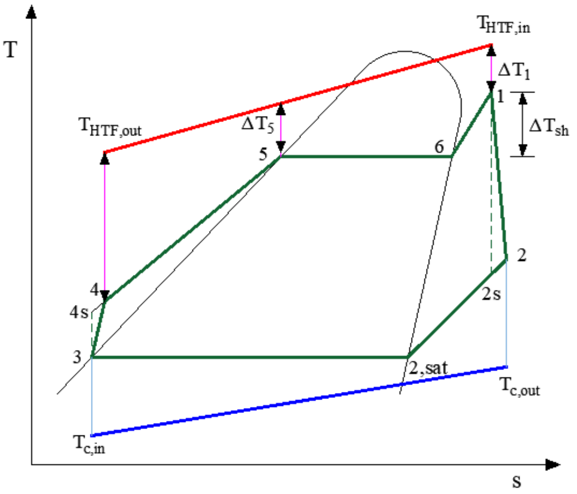

Figure 2. The T-s diagrams for the ORC system.

Applying the first and second laws of thermodynamics, the energy and exergy balance equations were used to evaluate the performance of the ORC system across a wide range of variables, as presented in Table 2. The mass, energy, and exergy balancing equations for components undergoing a steady flow process are provided in Eqs (11)–(13), assuming that the contributions of kinetic and potential energies are minimal and without considering the impacts of kinetic and potential exergies.

$$\sum \dot{m}_{wf,i} - \sum \dot{m}_{wf,e} = 0 \tag{11}$$

$$\dot{Q}_i - \dot{Q}_e + \dot{W}_i - \dot{W}_e + \dot{m}_{wf}\left[\sum h_i - \sum h_e\right] = 0 \tag{12}$$

$$\dot{E}_{ch} + \dot{Q}_i\left(1 - \frac{T_o}{T_s}\right)_i - \dot{Q}_e\left(1 - \frac{T_o}{T_s}\right)_e + \dot{W}_i - \dot{W}_e + \dot{m}_{wf}\left[\sum\left(h - T_o s\right)_i - \sum\left(h - T_o s\right)_e\right] - \dot{X}_d = 0 \tag{13}$$

where $\dot{m}_{wf}$ is the mass flow rate of the working fluid, $\dot{Q}$ is the heat transfer rate, $\dot{W}$ represents the work transfer rate, h is the flow specific enthalpy, s is the flow specific entropy, $\dot{X}_d$ is the exergy destruction, and i and e stand for the inlet and outlet of each component, respectively.

Table 2. The variables for ORC system performance.

S/N	Input parameter	Range
1	Biomass (Fuel)	1 (coconut shell) and 2 (cornstalk)
2	Mixture strength (Mx-Str), λ	40–75 (interval = 7)
3	Biomass consumption rate, $\dot{m}_{fuel}$ (kg/s)	0.05, 0.11, 0.22, 0.47 and 1.00
4	HTF Temperature change (ΔT_{HTF}) (K)	25–85 (interval = 20)
5	Upper cycle pressure, p_6 (MPa)	2.6–3.5 (interval = 0.225)
6	Turbine inlet temperature, T_1 (K)	$T_{sat}(p_6) + \Delta T_{\mathrm{sh}}$, ΔT_{sh} = 0–20 (interval = 5)
7	Lower cycle temperature, T_2 (K)	300–310 (interval = 2.5)
8	Pinch point temperature of evaporator, min (ΔT_1, ΔT_5), *ppt* (K)	5–20 (interval = 5) [39–41]
9	Pump efficiency, η_P (%)	75–90 (interval = 5) [39,42,43]
10	Turbine efficiency, η_T (%)	75–90 (interval = 5) [39,42,43]

Equations (11)–(13) were reduced for each component of the ORC system shown in Figure 1 to estimate the heat transfer rate, work rate, and exergy destruction rate (irreversibility) [44–47]. In this analysis, it was assumed that there were no heat losses, pressure drops, or mechanical losses during the expansion and compression processes. Thus, for the evaporator, the rate of heat transfer is equated with Eq (10), while also assuming no heat loss in the heat transfer circuit, that is

$$\dot{Q}_{eva} = \dot{Q}_{HTF} = \dot{m}_{wf}\left(h_1 - h_4\right) \tag{14}$$

and the rate of exergy destruction at the evaporator is determined as

$$\dot{X}_{d,eva} = \dot{m}_{HTF} c_{p,HTF}\left[\left(T_{HTF,i} - T_{HTF,e}\right) - T_0 \ln\frac{T_{HTF,i}}{T_{HTF,e}}\right] - \dot{m}_{wf}\left[\left(h_1 - h_4\right) - T_0\left(s_1 - s_4\right)\right] \tag{15}$$

Similarly, for the condenser, we have

$$\dot{Q}_{con} = \dot{m}_{wf}\left(h_2 - h_3\right) \tag{16}$$

$$\begin{aligned}\dot{X}_{d,con} = {} & \dot{m}_{wf}\left[\left(h_2 - h_3\right) - T_0\left(s_2 - s_3\right)\right] \\ & - \left[\dot{m}_{wf}\left(h_2 - h_{2sat}\right)\left(1 - \frac{T_0}{\left(T_2 + T_{2sat}\right)/2}\right) + \dot{m}_{wf}\left(h_{2sat} - h_3\right)\left(1 - \frac{T_0}{T_2}\right)\right]\end{aligned} \tag{17}$$

The rates of work transfer and exergy destruction for the turbine, respectively, are

$$\dot{W}_t = \eta_t \dot{m}_{wf}\left(h_1 - h_{2s}\right) \tag{18}$$

and

$$\dot{X}_{d,t} = \dot{m}_{wf}\left[\left(h_1 - h_2\right) - T_0\left(s_1 - s_2\right)\right] \tag{19}$$

Lastly, for the pump, they are

$$\dot{W}_p = \dot{m}_{wf}\left(h_{4s} - h_3\right)/\eta_p \tag{20}$$

and

$$\dot{X}_{d,p} = \dot{m}_{wf}\left[\left(h_4 - h_3\right) - T_o\left(s_4 - s_3\right)\right] \tag{21}$$

The net output power generated by the system is calculated from

$$\dot{W}_{net} = \dot{W}_t - \dot{W}_p \tag{22}$$

while the cycle efficiency of the ORC unit is given by

$$\eta_{cycle} = \frac{\dot{W}_{net}}{\dot{Q}_{eva}} \tag{23}$$

The chemical exergy rate (kW) of biomass is computed using an empirical correlation as [48],

$$\dot{E}_{ch} = \dot{m}_{fuel}(1812.5 + 295.606C + 587.354H + 17.506O + 17.735N + 95.615S - 31.8c_A) \tag{24}$$

The exergy transfer by the flue gas to the heat transfer fluid was then estimated from

$$\dot{E}_{fg} = \dot{m}_{fg}c_{p,fg}\left[\left(T_{fg,i} - T_{fg,e}\right) - T_0 \ln\frac{T_{fg,i}}{T_{fg,e}}\right] \tag{25}$$

while the exergy transferred from the HTF stream in the evaporator is expressed as

$$\dot{E}_{HTF} = \dot{m}_{HTF}c_{p,HTF}\left[\left(T_{HTF,i} - T_{HTF,e}\right) - T_0 \ln\frac{T_{HTF,i}}{T_{HTF,e}}\right] \tag{26}$$

Then, exergy efficiency, which is the fraction of the available exergy converted to useful exergy, was determined for each of the ORC circuit, HTF–ORC, and the whole biomass-ORC plant, respectively, as

$$\eta_{ex,ORC} = \frac{\dot{W}_{net}}{\dot{E}_{HTF}} \tag{27}$$

$$\eta_{ex,HTF-ORC} = \frac{\dot{W}_{net}}{\dot{E}_{fg}} \tag{28}$$

and

$$\eta_{ex,Pl} = \frac{\dot{W}_{net}}{\dot{E}_{ch}} \tag{29}$$

2.3. Data cleaning and preprocessing

The comprehensive dataset of 1,920,000 data points generated from the thermodynamic analysis was cleaned in MATLAB to improve its quality and ensure a reliable analysis. Filtering the outliers, the data points were reduced to 483,840 rows of the dataset. This was followed by a scaling transformation of the input features to a 0–1 range using z-score normalization to ensure faster convergence and reduce the impact of feature magnitude disparities among the features and within the data obtained for each feature. The normalization was performed using

$$z = \frac{x - \mu}{\sigma} \tag{30}$$

where z is the normalized value, x represents the original data point, μ is the mean of column data, and σ stands for the standard deviation.

The dataset was randomly shuffled and split into training (80%), validation (10%), and testing (10%) subsets. The division was done to allow unbiased performance evaluation and mitigate overfitting risks. The DNN model was developed in MATLAB using the feedforward architecture suitable for regression tasks. As depicted in Figure 3, the network comprised an input layer with 9 neurons representing the input features, followed by three hidden layers, and a final regression output layer with four neurons corresponding to the four target variables, that is, the net output power, cycle efficiency, exergy efficiency of the HTF–ORC, and exergy efficiency of the biomass plant.

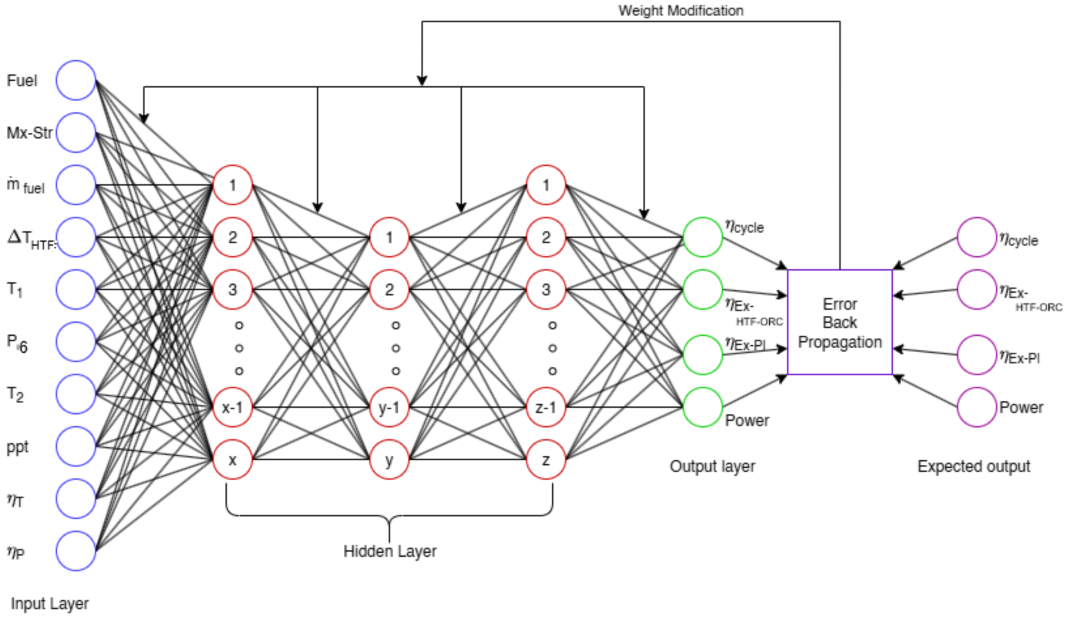

Figure 3. Model architecture of the DNN.

2.4. Activation function and hyperparameter tuning

The hidden layers were structured to include batch normalization, non-linear activation functions, such as ReLU, ELU, sigmoid, tanh, and LRELU, and a dropout layer with a 20% dropout rate to prevent overfitting by randomly deactivating neurons during training [49,50]. The L2 regularization was also used with a weight decay coefficient of 0.01 to penalize large weights while reducing the impact of overfitting. Batch normalization was used to limit internal covariate shift to speed up and stabilize training [51]. The fully connected layers had different neuron counts with 64, 128, and 256 units tested for optimal performance. The network used the Adam optimizer, a stochastic gradient descent-based optimizer that is highly effective for large and noisy datasets with adaptive learning rates and momentum [52,53]. The model was trained for up to 100 epochs, while varying batch sizes of 64, 128, 256 to balance learning stability with training speed. The initial learning rate was 0.001, decaying using a piecewise schedule with a drop factor of 0.5 every 10 epochs continuing to convergence without stalling. The learning decay strategy allows for larger updates, early in training, which become more fine-tuned as the model converges to ensure that oscillations are around the minimum [53,54]. The validation dataset was used during training to keep an account of generalization performance every 30 iterations.

2.5. Model evaluation metrics

The performance of the trained model was evaluated using multiple metrics for performance, including the root mean square error (RMSE), mean absolute error (MAE), normalized root mean-square error (NRMSE), coefficient of determination (R^2), mean absolute percentage error (MAPE), average absolute deviation (AAD), and average percent deviation (bias). These metrics were used to assess the level of precision of prediction, robustness, and explanatory power, and are defined as follows:

$$RMSE = \sqrt{\frac{1}{n}\sum_{i=1}^{n}\left(y_i - \hat{y}_i\right)^2} \tag{31}$$

$$MAE = \frac{1}{n}\sum_{i=1}^{n}\left|y_i - \hat{y}_i\right| \tag{32}$$

$$NRMSE = \frac{RMSE}{y_{\max} - y_{\min}} \tag{33}$$

$$R^2 = 1 - \frac{\sum_{i=1}^{n}\left(y_i - \hat{y}_i\right)^2}{\sum_{i=1}^{n}\left(y_i - \bar{y}_i\right)^2} \tag{34}$$

$$MAPE = \frac{100}{n}\sum_{i=1}^{n}\left|\frac{y_i - \hat{y}_i}{y_i}\right| \tag{35}$$

$$AAD = \frac{100}{n}\frac{\sum_{i=1}^{n}\left|y_i - \hat{y}_i\right|}{\bar{y}} \tag{36}$$

$$Bias = \frac{1}{n}\sum_{i=1}^{n}\left(y_i - \hat{y}_i\right) \tag{37}$$

where y_i is the actual value, $\hat{y}_i$ is the predicted value, $\bar{y}_i$ is the mean of the observed values, and n represents the number of data points [55–58].

2.6. Multi-objective optimization with PSO and TOPSIS

The existence of four different output features of interest: net power output, cycle efficiency, and exergy efficiencies of the HTF–ORC and overall biomass-ORC system requires a multi-objective optimization framework that properly addresses their trade-offs. The objectives are often conflicting in nature; for example, maximizing power output often results in decreased exergy efficiency. To do this, Pareto-based optimization was performed using PSO to search for a collection of non-dominated solutions. PSO is a population-based stochastic optimization method that is based on the social behavior of birds flocking or fish schooling. PSO has also been proven to be efficient at solving multi-objective engineering problems due to the relative ease of the method and the ability to converge on the global optimum with fewer parameters [59,60]. Each particle in the swarm acts as a potential solution, updating its velocity and position based on its own experience combined with the experience of its neighbors:

$$v_i(t+1) = wv_i(t) + c_1r_1\left[p_i(t) - x_i(t)\right] + c_2r_2\left[g_i(t) - x_i(t)\right] \tag{38}$$

$$x_i(t+1) = x_i(t) + v_i(t+1) \tag{39}$$

where w is the initial weight, c_1 and c_2 are acceleration coefficients, r_1 and r_2 are random numbers uniformly distributed in [0,1], p_i is the particle's personal best position, and g_i is the leader selected for particle i from the non-dominated solutions [61,62]. Based on the range of values reported in the literature, w = 0.4 and c_1 = c_2 = 1.5 were adopted for this analysis. Also, the algorithm was implemented with a swarm size of 50 particles and iterated over 100 generations to achieve convergence. The multi-objective optimization problem is then formulated as

$$max \quad f(x) = \left[\dot{W}_{net},\ \eta_{cycle},\ \eta_{ex,HTF-ORC},\ \eta_{ex,Pl}\right]$$

where the input variables are described as the decision vector

$$x = \left[Fuel,\ \lambda,\ \dot{m}_{fuel},\ T_1,\ p_6,\ T_2,\ ppt,\ \eta_P,\ \eta_T\right]$$

and these were constrained to the upper and lower bounds as presented in Table 2.

The fitness function integrated all four output features, guiding the swarm toward a set of non-dominated solutions that constitute the Pareto front. To select the most suitable configuration from the Pareto front, TOPSIS was applied [63,64]. TOPSIS identifies the ideal (A^+) and anti-ideal (A^-) solutions, which are defined as [65–67].

$$A^+ = \left\{v_1^+, v_2^+, \ldots, v_m^+\right\} \tag{40a}$$

$$A^- = \left\{v_1^-, v_2^-, \ldots, v_m^-\right\} \tag{40b}$$

Then, the separation measure is calculated as the Euclidean distance from each alternative rating to these benchmarks as

$$S_i^+ = \sqrt{\sum_{j=1}^{m}\left(v_{ij} - v_j^+\right)^2} \tag{41a}$$

$$S_i^- = \sqrt{\sum_{j=1}^{m}\left(v_{ij} - v_j^-\right)^2} \tag{41b}$$

where v_{ij} are the normalized values in the decision matrix, and v_j^+ and v_j^- denote the ideal and anti-ideal values, respectively. The relative closeness to the ideal solution is then calculated as

$$C_i = \frac{S_i^-}{S_i^+ + S_i^-} \tag{42}$$

with the solution exhibiting the highest C_i is deemed most preferable.

2.7. Parameter selection using the Spearman rank correlation coefficient

Figure 4 illustrates the Spearman rank correlation coefficient among the four thermodynamic performance indicators derived from the combustion and thermodynamic analyses. The Spearman rank correlation is a nonparametric technique that does not presuppose a particular distribution of the population. This approach is especially beneficial for ordinal data or in cases where linearity and normality assumptions are not met [68,69]. The Spearman rank correlation coefficient varies between −1 and +1, with +1 signifying a perfect positive monotonic relationship and −1 signifying a perfect negative monotonic relationship. The figure clearly indicates that some parameters exhibit no correlation (zero coefficient) with specific output variables. Notably, the temperature difference of the heat transfer fluid, ΔT_{HTF}, demonstrated a zero-correlation coefficient with all output features.

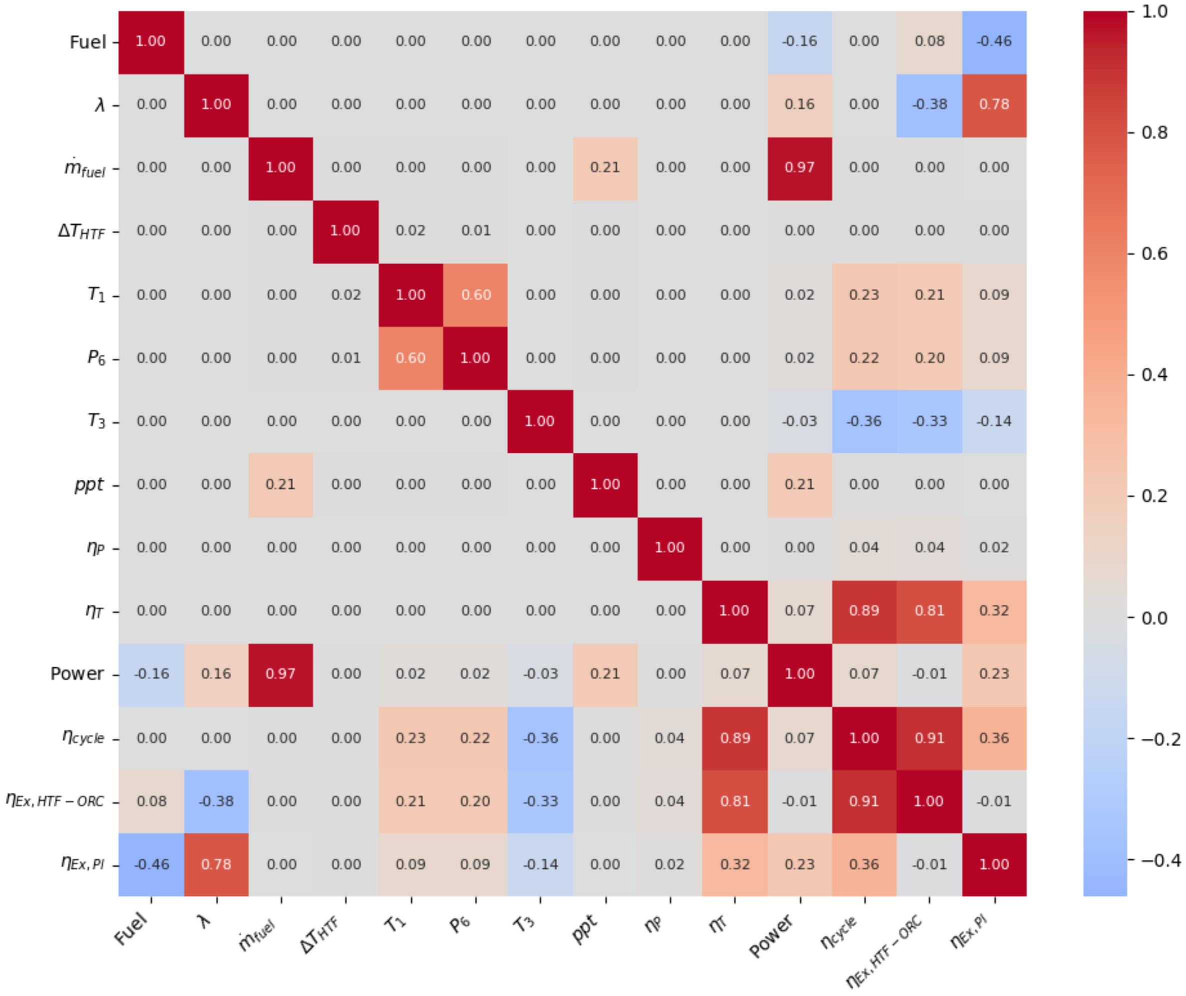

	Fuel	λ	$\dot{m}_{fuel}$	ΔT_{HTF}	T_1	P_6	T_3	ppt	η_P	η_T	Power	η_{cycle}	$\eta_{Ex,HTF-ORC}$	$\eta_{Ex,PI}$
Fuel	1.00	0.00	0.00	0.00	0.00	0.00	0.00	0.00	0.00	0.00	-0.16	0.00	0.08	-0.46
λ	0.00	1.00	0.00	0.00	0.00	0.00	0.00	0.00	0.00	0.00	0.16	0.00	-0.38	0.78
$\dot{m}_{fuel}$	0.00	0.00	1.00	0.00	0.00	0.00	0.00	0.21	0.00	0.00	0.97	0.00	0.00	0.00
ΔT_{HTF}	0.00	0.00	0.00	1.00	0.02	0.01	0.00	0.00	0.00	0.00	0.00	0.00	0.00	0.00
T_1	0.00	0.00	0.00	0.02	1.00	0.60	0.00	0.00	0.00	0.00	0.02	0.23	0.21	0.09
P_6	0.00	0.00	0.00	0.01	0.60	1.00	0.00	0.00	0.00	0.00	0.02	0.22	0.20	0.09
T_3	0.00	0.00	0.00	0.00	0.00	0.00	1.00	0.00	0.00	0.00	-0.03	-0.36	-0.33	-0.14
ppt	0.00	0.00	0.21	0.00	0.00	0.00	0.00	1.00	0.00	0.00	0.21	0.00	0.00	0.00
η_P	0.00	0.00	0.00	0.00	0.00	0.00	0.00	0.00	1.00	0.00	0.00	0.04	0.04	0.02
η_T	0.00	0.00	0.00	0.00	0.00	0.00	0.00	0.00	0.00	1.00	0.07	0.89	0.81	0.32
Power	-0.16	0.16	0.97	0.00	0.02	0.02	-0.03	0.21	0.00	0.07	1.00	0.07	-0.01	0.23
η_{cycle}	0.00	0.00	0.00	0.00	0.23	0.22	-0.36	0.00	0.04	0.89	0.07	1.00	0.91	0.36
$\eta_{Ex,HTF-ORC}$	0.08	-0.38	0.00	0.00	0.21	0.20	-0.33	0.00	0.04	0.81	-0.01	0.91	1.00	-0.01
$\eta_{Ex,PI}$	-0.46	0.78	0.00	0.00	0.09	0.09	-0.14	0.00	0.02	0.32	0.23	0.36	-0.01	1.00

Figure 4. The Spearman correlation heatmap.

Additionally, the p-value, obtained alongside the Spearman rank coefficient, indicated that input parameters with a p-value less than 0.001 were correlated with the output variables [70,71]. As shown in Table 3, only ΔT_{HTF} exhibited p-values exceeding 0.001 for all output features. This indicates a failure to reject the null hypothesis, demonstrating a lack of correlation with any of the output features, and, therefore, ΔT_{HTF} was not included in the deep learning analysis. This is partly because the heat transfer fluid was used to stabilize and convey the thermal energy removed from the flue gas to the working fluid. Changes in ΔT_{HTF} were offset by variations in the flow rate of the heat transfer fluid to maintain consistent thermal energy transfer, although it only affects the stream temperatures on the hot side of the evaporator.

Table 3. The p-values of the relationship between the input parameters and performance indicators.

Indicator	Fuel	Mx-Str	$\dot{m}_{fuel}$	$\Delta \mathrm{T}_{\mathrm{HTF}}$	T_1	P_6	T_2	*ppt*	η_{P}	η_{T}
Power	0.0	0.0	0.0	0.002788	0.0	0.0	0.0	0.0000	0.00197	0.0
η_{cycle}	1.0	1.0	0.2759	0.001360	0.0	0.0	0.0	0.5378	0.0	0.0
$\eta_{\mathrm{Ex\_HTF–ORC}}$	0.0	0.0	0.3201	0.003472	0.0	0.0	0.0	0.5740	0.0	0.0
$\eta_{\mathrm{Ex\_Pl}}$	0.0	0.0	0.6834	0.230500	0.0	0.0	0.0	0.8176	0.0	0.0

The violin plot in Figure 5 presents the kernel density distributions of the data obtained for the performance indicators for the coconut shell and cornstalk to offer insight into their magnitudes and variabilities. The wider sections represent the region of higher concentrations in the estimates, while the narrower sections represent values with fewer frequencies. The statistical measures, including the minimum, maximum, mean, median, and percentiles for each distribution, have also provided more comprehensive insight into the central tendency and distribution shape of each of the thermodynamic indicators. The variations observed in the distributions have also indicated the greater influence of the biomass type on the performance indicators, except for the cycle efficiency, which is only a measure of how the heat input to the ORC circuit is converted into useful work output.

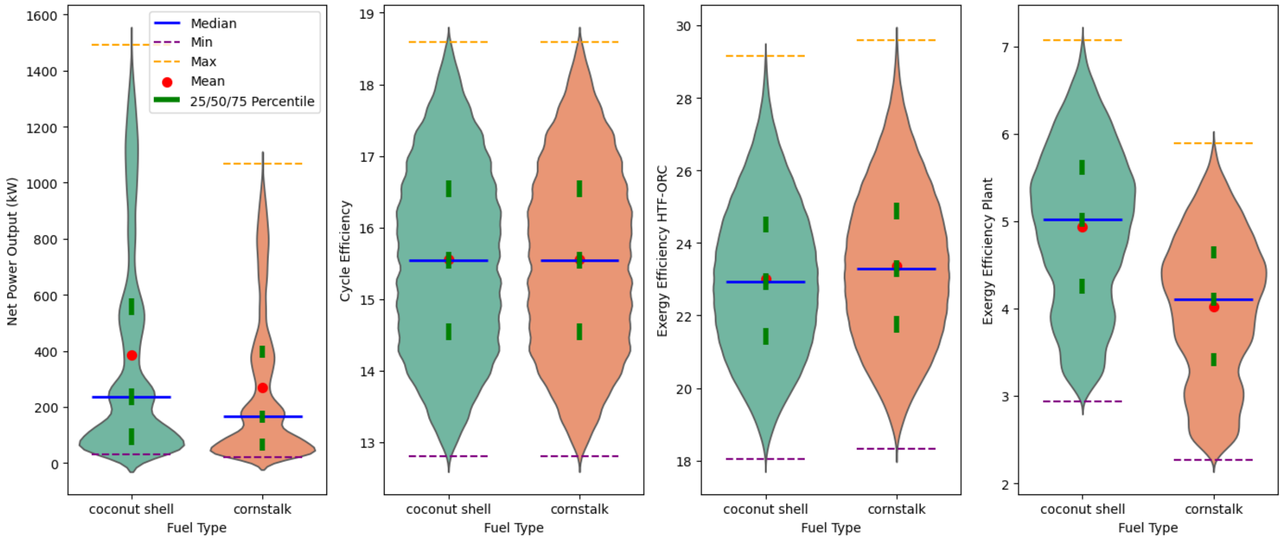

Figure 5. The kernel density distributions of the data.

2.8. Model validation

In order to validate the stoichiometric combustion analysis of biomass, the process was replicated for methane and validated using a customized combustion model based on Gibbs free energy minimization with GRI-Mech 3.0 species from Cantera. Cantera is a benchmarked, open-source suite of tools for problems involving thermodynamics, chemical kinetics, and transport phenomena. Methane was used because there is no built-in support structure for biomass in Cantera [72–74]. AFT of the stoichiometric model with the Cantera combustion model is shown in Figure 6. It is clearly shown in this figure that there is an excellent agreement between the stoichiometric combustion analysis and the customized combustion model by Cantera, with a variation of 5% for the range of equivalent ratio (mixture strength) considered. The small variation is expected because the stoichiometric combustion analysis is a simplified approach compared to the Gibbs free energy minimisation. Besides, the LHV for methane (C: 74.87%, H: 25.13%) calculated to be 50.15 MJ/kg is approximately the same as the 50.03 MJ/kg determined from the Cantera model. Moreover, to validate the thermodynamic analysis conducted in MATLAB using CoolProp to evaluate the cycle efficiency of the biomass-powered ORC, comparative simulations were performed with Engineering Equation Solver (EES) and DWSIM, a chemical process simulator [75].

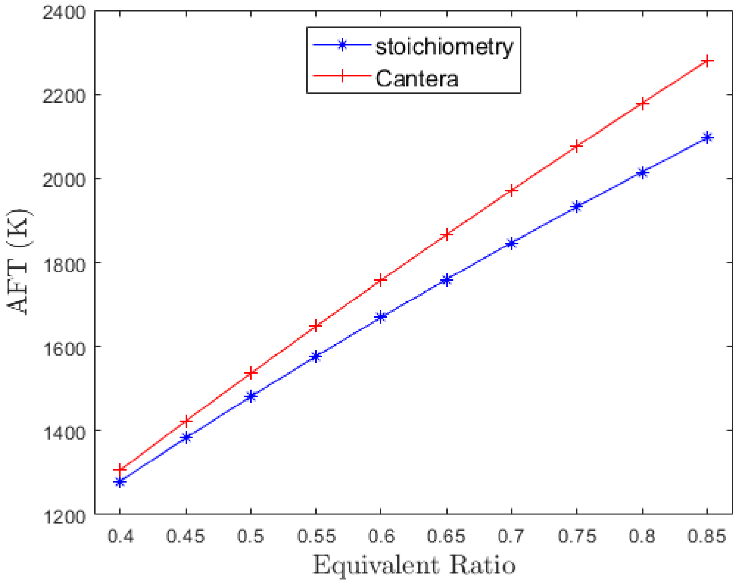

Figure 6. AFT.

As shown in Figure 7, the variations of cycle efficiencies with the upper cycle pressure exhibited a discrepancy of only 0.78% when compared to EES and 2.31% in relation to DWSIM, indicating a robust agreement across all platforms. These small discrepancies could be due to differences in the fluid property libraries, numerical methods, and solver algorithms used by each piece of software. The results are consistent, which shows that the MATLAB-based analysis is accurate and reliable.

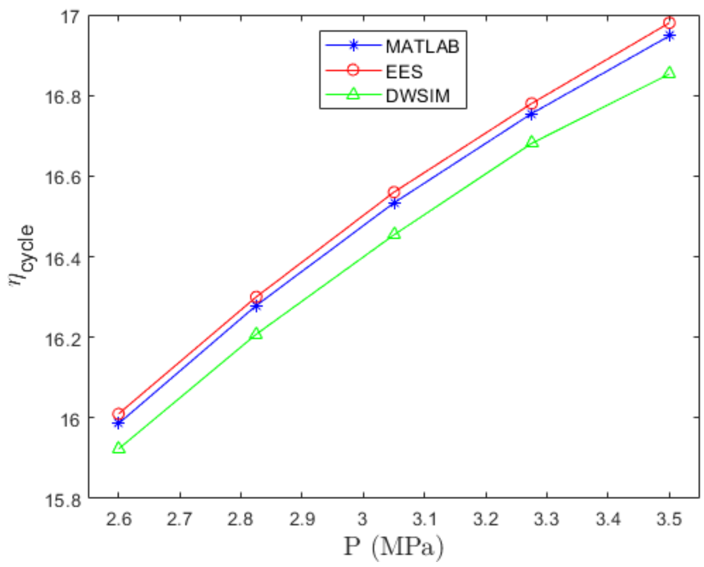

Figure 7. The influence of the upper cycle pressure on cycle efficiency.

3. Results and discussion

3.1. Performance of activation functions

The performance metrics of different activation functions (ReLU, ELU, Sigmoid, Tanh, and Leaky ReLU) for predicting the power output, cycle efficiency, and exergy efficiencies of the HTF–ORC and entire biomass-ORC plant are shown in Figure 8. The analysis employs RMSE, MSE, NRMSE, MAE, R^2, MAPE, AAD, bias, and accuracy metrics for comparison.

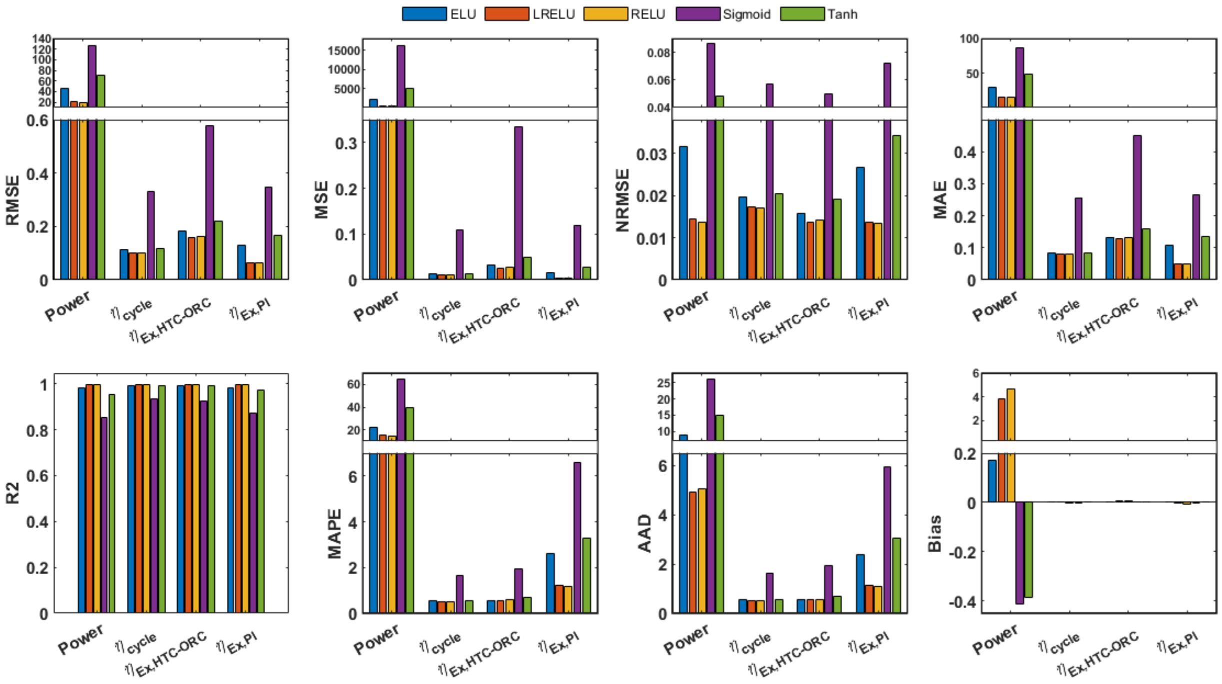

Figure 8. The performance metrics for various activation functions.

The results of deep learning analyzed through these target variables all indicate ReLU was consistently more accurate in predictions than any of the other activation functions. In power output predictions, ReLU achieved the lowest RMSE (20.1610) and MSE (406.4676) along with the highest R^2 value (0.9962) compared to other activation functions. LReLU also performed similarly with RMSE of 21.1671. Tanh and Sigmoid both had RMSE values that were significantly higher than ReLU and LReLU, at 70.7294 and 126.7968 respectively, indicating it was not as accurate. A similar trend was observed for thermal efficiency predictions, with ReLU producing the most accurate prediction (RMSE: 0.0990) compared with LReLU (RMSE: 0.1004), which was better than ELU (RMSE: 0.1136), Tanh (RMSE: 0.118), and Sigmoid (RMSE: 0.3296).

On the exergy-related metrics, ReLU outperformed the others, achieving an RMSE = 0.0643 for overall plant exergy efficiency, with LReLU not far behind with RMSE = 0.0654. For flue-ORC exergy efficiency, LReLU (RMSE = 0.1579) slightly outperformed ReLU (RMSE = 0.1629), with both exhibiting high R^2 values (0.9939 and 0.9943). Sigmoid and Tanh performed the least well across all categories, as demonstrated by their high RMSE and low R^2. These findings suggest that ReLU is the best activation function for accurately predicting the nonlinear performance of ORC systems, while LReLU performed comparably in certain cases. The greater RMSE, MAE, and MSE values for power output compared to efficiency metrics can be explained by different scales of the output variable. However, the same patterns were not present in scale-independent metrics like R^2 and nRMSE, which exhibited the same model performance across outputs.

Figure 9 presents the losses, training, validation, and test results of the various activation functions. Overall, ReLU had the lowest average loss comparison (training = 0.005088, validation = 0.005109, test = 0.005066), followed by Leaky ReLU, which had the second lowest overall loss (training = 0.005151, validation = 0.005179, test = 0.005157 for Leaky ReLU). Together, these results demonstrate ReLU and Leaky ReLU performed well in the model's generalization in all predictions across categories.

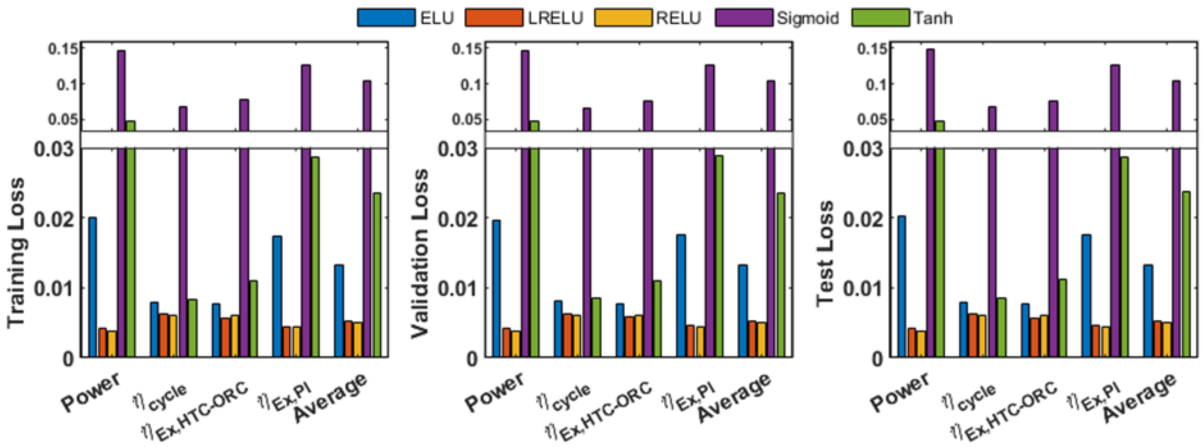

Figure 9. The losses associated with the activation functions.

On the contrary, both ELU and Tanh had moderately higher losses than those noted previously (0.01334 and 0.02370, for Tanh and ELU, respectively), and Sigmoid had the highest average test loss of 0.105, which suggests poorer predictive accuracy and potential vanishing gradients. However, it is obvious to note that the training, validation and test losses are almost equal within the different activation functions, indicating all models did not demonstrate underfitting or overfitting tendencies demonstrated as reliability within the metrics reported. Overall, it seems ReLU and Leaky ReLU, of the activation functions tested, should present the best reliability for predicting ORC. The close alignment between training, validation, and test losses across all functions indicates that the models avoided both underfitting and overfitting, with ReLU and Leaky ReLU emerging as the most reliable activations for ORC prediction.

3.2. Performance of the fully connected hidden layers

The analysis was performed with RELU as the activation function, a batch size of 128, and a learning rate of 0.001 across various network architectures that included three hidden layers (for instance, 128-64-64 neurons). Figure 10 demonstrates the capabilities of the models in predicting the power output, thermal efficiency, and exergy efficiencies of the ORC.

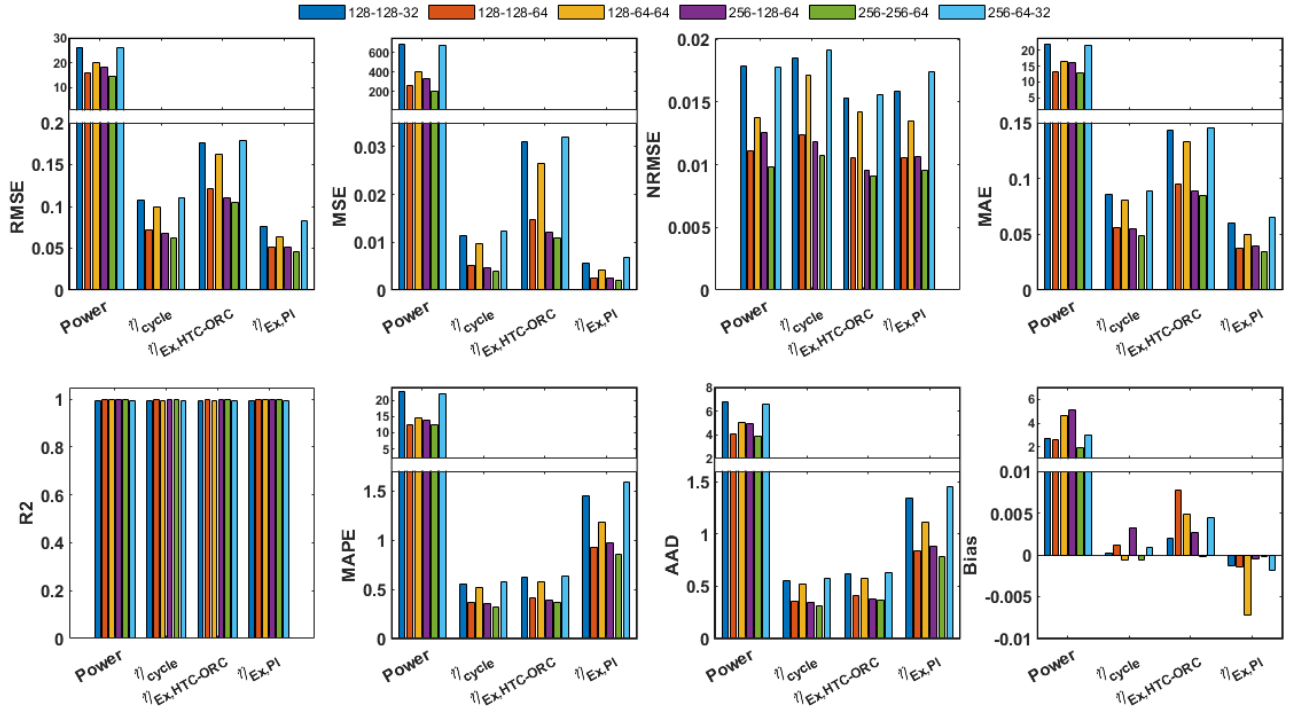

Figure 10. The performance metrics and hidden layer neurons.

Overall, the results indicate that deeper and wider networks increased accuracy as well. The best-performing model for power output was the 256-256-64 network (RMSE = 14.3834, $R^2 = 0.9981$), while smaller models such as the 128-128-32 and 256-64-32 networks had higher error ranges (RMSE = 26.1818 and 26.0620). This trend was also evident in other metrics. The 256-256-64 model also exhibited the best performance for thermal efficiency (RMSE = 0.06199), HTF–ORC exergy efficiency (RMSE = 0.1047), and overall plant efficiency (RMSE = 0.04573). Conversely, the less complicated networks performed poorly, with much larger error margins. The results reveal that deeper network structures provided meaningful advantages for learning the nonlinear processes governing ORC systems, and also produced meaningful and reliable predictions. However, it is also worth noting that computational cost increases with model complexity, with the largest network (256-256-64) requiring 4 hours 32 minutes of training time compared to approximately 3 hours 52 minutes for the smallest architecture (128-64-64) on an Intel(R) Core (TM) i7-8750H CPU @ 2.20 GHz workstation.

The network performance was evaluated for the hidden layers. The results indicated that the deeper and wider networks generally had improved accuracy (Figure 11). The 256-256-64 network had the lowest losses across all outputs (average test loss = 0.001923 for power output, 0.002368 for thermal efficiency, 0.002213 for exergy efficiency of HTF_ORC, and 0.002254 for plant exergy efficiency), followed closely by the 256-128-64 network. Conversely, smaller networks, such as 128-64-64 and 128-128-32, had higher test losses on average of 0.005066 and 0.006652, respectively, indicating less predictive capability. Additionally, the training, validation, and test losses were consistently close across all cases, suggesting the models were well-generalized, with no underfitting or overfitting identified.

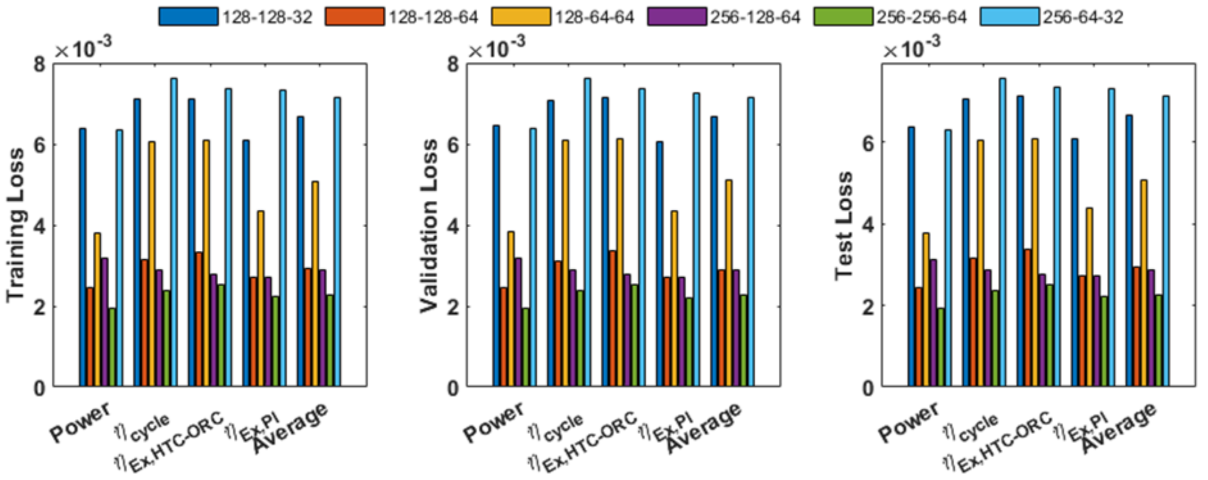

Figure 11. The losses for varying hidden layer neurons.

3.3. Prediction performance for hyperparameter tuning

Figure 12 illustrates the performance of the hidden layer architecture 256-256-64 with respect to learning rate and batch size. There were three batch sizes (64, 128, and 256) and three initial learning rates (0.1, 0.01, and 0.001), which were adjusted adaptively with a 0.5 drop factor every 10 epochs. When the learning rate was at the highest rate, 0.1, the model resulted in larger errors as indicated for 128-0.1 with RMSE = 80.4650 and $R^2 = 0.9395$ for power output. At a learning rate of 0.01, there was a considerable change in performance. For power output, the RMSE dropped to 13.0142, and R^2 increased to 0.9984. The learning rate of 0.001 marginally trailed behind the learning rate at 0.01 for power output, with RMSE = 14.3834 and $R^2 = 0.9981$. However, its predictions for the other three output features were better and more stable.

Also, a batch size of 128 provided the most balanced and reliable learning behavior compared to smaller (64) and larger (256) sizes, which, although competitive, showed slightly higher errors and less stable convergence. Hence, the combination of learning rate 0.001 and batch size 128 was optimal, producing the lowest losses and highest predictive accuracy across power output, thermal efficiency, and the exergy efficiencies.

The results of the loss, as indicated in Figure 13, provide very clear evidence of the importance of learning rate and batch size in determining model performance. The average losses for the learning rate at 128-0.1 were 0.0751, and this confirms that updates were unstable and could not converge adequately. Reducing the learning rate parameter to 0.01 provided a large drop of 0.00345 in loss, while the learning rate of 0.001 produced the most consistent performance for the study, averaging at 0.00226 across training, validation, and test sets. The batch size also matters, as the learning rate parameters of 64-0.001 and 256-0.001 produced almost the same averaged loss values, but demonstrated a very slight instability in learning, relative to the 128-0.001 run. Again, these findings align well with the previous trends for performance metrics, reinforcing not only that the combination of 128-0.001 was the most balanced in terms of performance, accuracy, and stability, but also that there are no signs of the model showing overfitting or underfitting.

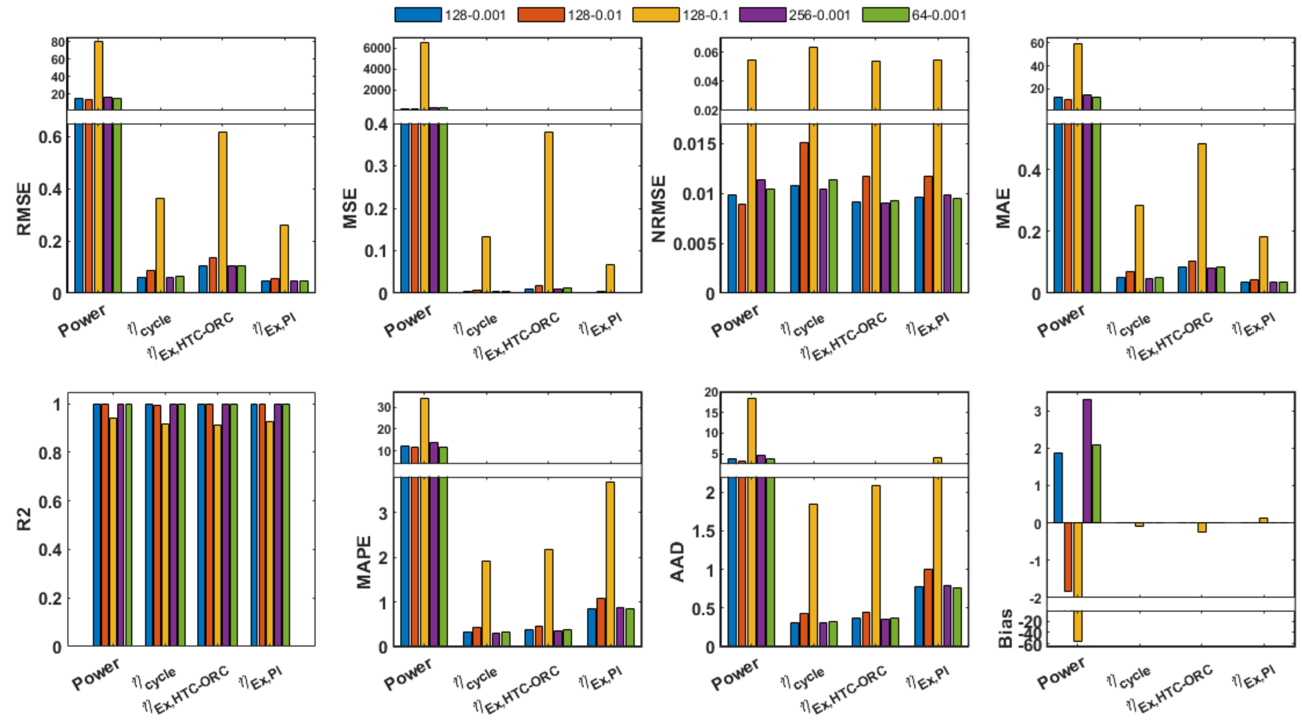

Figure 12. The performance metrics for hyperparameter tuning.

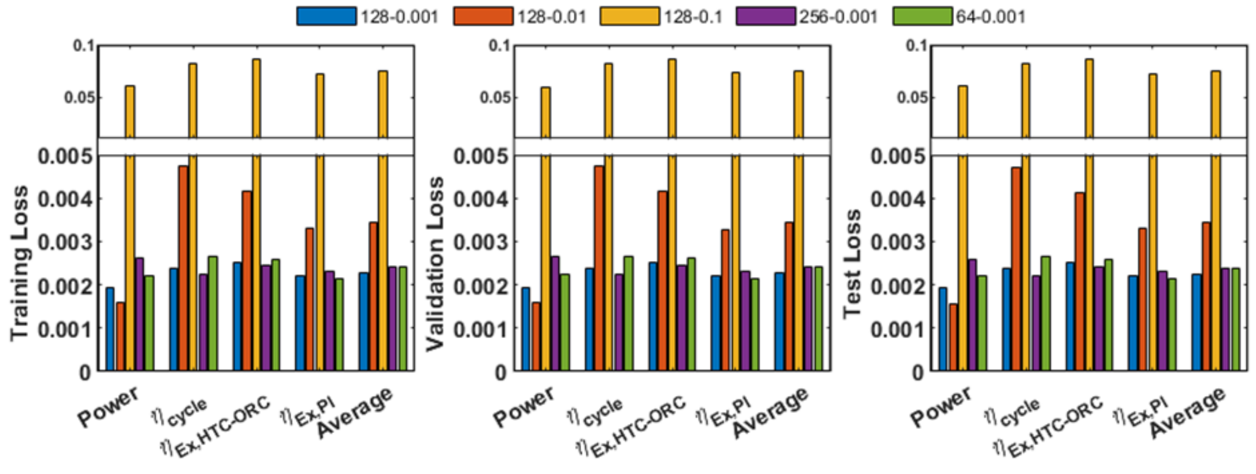

Figure 13. The losses for hyperparameter tuning.

3.4. Model prediction deviations

Figure 14 shows the deviations between predicted values and actual values across the dataset for each of the four outputs of the ORC model, for the best-performing configuration of three hidden layers (256-256-64) trained using a batch size of 128 and a learning rate of 0.001. As mentioned before, this selection of hyperparameters offered the most stable and accurate predictions among all the tested cases.

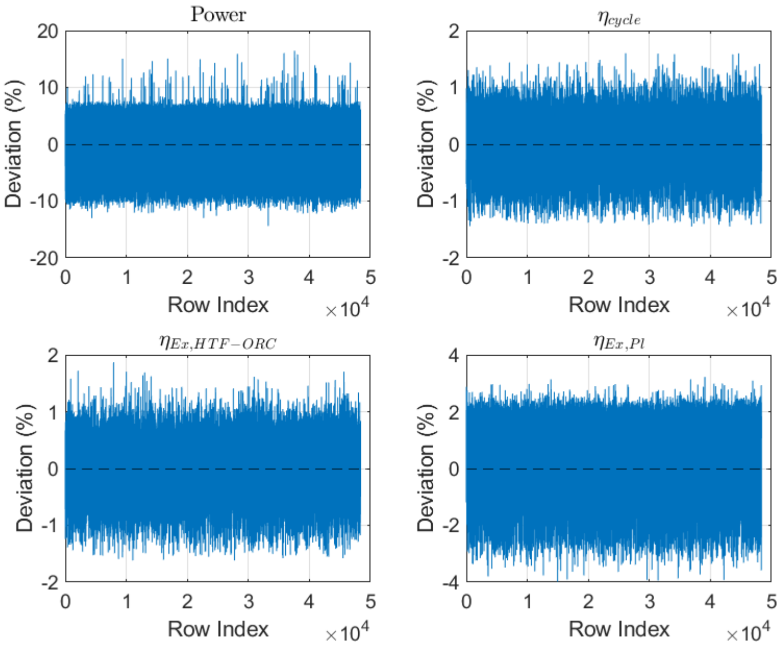

Figure 14. The deviations between actual and predicted values.

For power output (top-left), the deviations are spread within ±15–16%, with the majority clustered around zero, showing that the model effectively captures large-scale variations despite the wider spread relative to efficiency indicators. By contrast, the cycle efficiency (top-right) and the exergy efficiency of the HTF–ORC (bottom-left) exhibit far tighter distributions, generally confined within ±1.5%, reflecting the model's high reliability in predicting efficiency-related outputs. The exergy efficiency of the overall biomass plant (bottom-right) shows slightly wider fluctuations (within ±2–3%) but remains well-centered, indicating consistent generalization.

From the nearly symmetrical distribution of the difference from the zero line, it can be inferred there is no systematic bias, and through the bounded spread, we observe no severe underfitting or overfitting in the output. Thus, the analysis confirms the previous observation that there is a fair amount of confidence in the predictions made with the selected architecture and hyperparameters for non-linear mapping of all output and prediction categories concerning ORC performance.

Figure 15 presents the comparison of actual and predicted values for the four output features of the ORC model, power output, cycle efficiency, exergy efficiency of the HTF–ORC, and exergy efficiency of the biomass plant, using the configuration with three hidden layers (256-256-64), batch size 128, and learning rate 0.001. The scatter plots show the predicted points (red) closely aligned with the diagonal line (blue), confirming that the model captures the nonlinear behavior of the ORC with minimal deviation.

The power output (upper left) exhibited some degree of dispersion over the wide range of outputs associated with the higher output values, but those deviated values remained in alignment, highlighting the robustness of the model even at higher outputs. However, the cycle efficiency (upper right), HTF–ORC exergy efficiency (lower left), and biomass plant exergy efficiency (lower right) demonstrate even tighter clustering along the diagonal, which confirms a more accurate prediction.

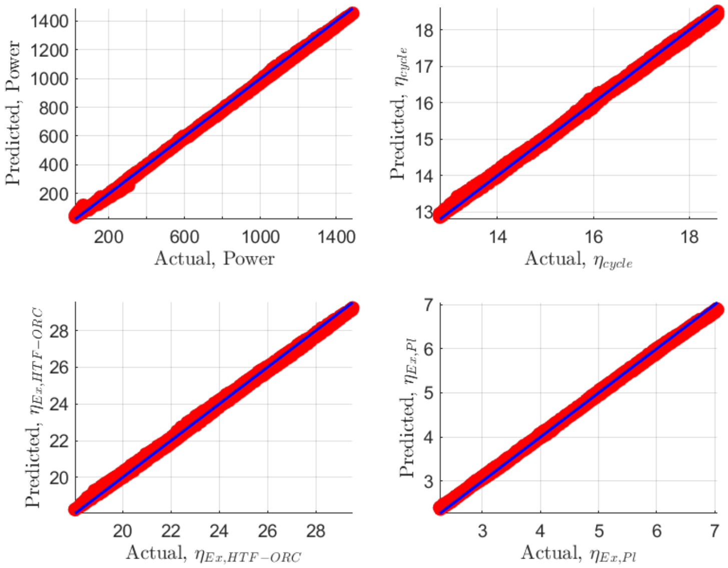

Figure 15. The comparison between the actual and predicted.

Overall, the figure reinforces the earlier conclusion that the selected architecture and hyperparameters achieve reliable performance across different ORC indicators, with especially strong agreement for efficiency-based features where deviations are smallest.

3.5. Pareto front from DNN optimization

The analyses performed in the preceding sections indicate that the operating parameters significantly influence overall system performance. An appropriate selection of operating parameters can significantly enhance system performance, which serves as an important evaluation indicator in practical engineering applications. The results of the optimal design points derived from Pareto-based optimization utilizing PSO for non-dominated solutions of the ORC system for the best-performed deep learning model are presented in Figure 16. Each subplot represents the same Pareto-optimal solution set projected in a different objective space, where three objectives are shown along the axes and the fourth is represented by the color scale. The plots reveal clear trade-offs across the objectives. In particular, higher power is generally linked to reduced HTF–ORC exergy efficiency, while having no significant change with the cycle efficiency. At the same time, maximizing plant exergy efficiency is typically associated with lower HTF–ORC efficiency but at a higher power output. The distribution of points highlights that efficiency gains often come at the cost of output, while higher power demands compromise efficiency. The results underline the importance of selecting operating conditions based on specific performance priorities, whether the focus is on maximizing output, improving efficiency, or finding a compromise between the two.

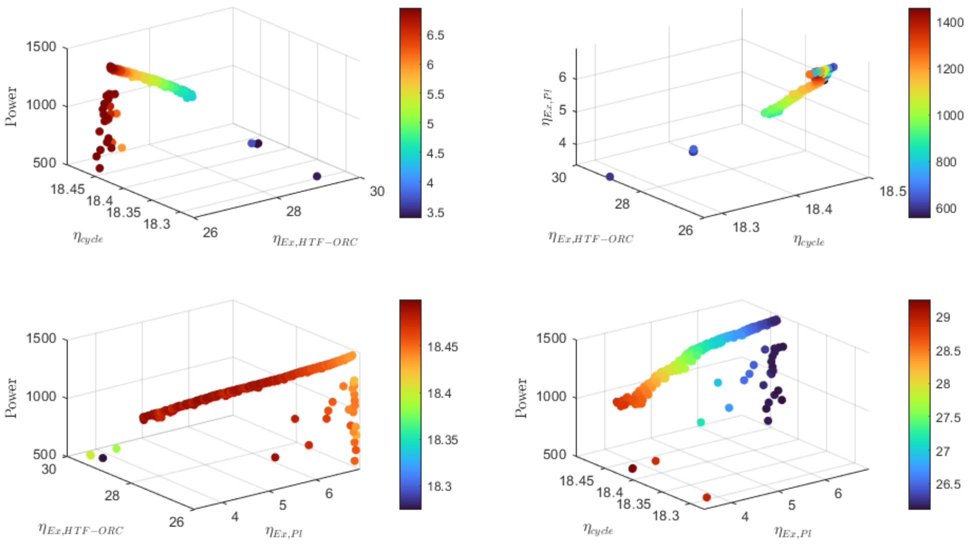

Figure 16. The Pareto front of the performance indicators.

3.6. TOPSIS ranking of Pareto front

Following the generation of the Pareto front, TOPSIS was applied to identify the most suitable design configurations based on four weight sets (0.25:0.25:0.25:0.25; 0.40:0.20:0.10:0.30; 0.10:0.40:0.40:0.10; and 0.30:0.10:0.40:0.20) as seen in Table 4. The weight sets were defined to reflect varying decision-making priorities across the four objectives, allowing assessment of how different preference structures influence TOPSIS ranking.

Table 4. TOPSIS ranking of the Pareto optimal solutions for different weights.

Fuel	Mx-Str, λ	$\dot{m}_{fuel}$	T_1	P_6	T_2	*ppt*	η_P	η_T
w = 0.25:0.25:0.25:0.25: (Power = 1460.54, η_{cycle} = 18.44, $\eta_{Ex,HTF-ORC}$ = 26.19, η_{Ex-PI} = 6.90)								
1	75.00	1.00023	444.68	3500000	300.15	20	0.9	0.9
w = 0.40:0.20:0.10:0.30: (Powe r = 1460.54, η_{cycle} = 18.44, $\eta_{Ex,HTF-ORC}$ = 26.19, η_{Ex-PI} = 6.90)								
1	75.00	1.00023	444.68	3500000	300.15	20	0.9	0.9
w = 0.10:0.40:0.40:0.10: (Power = 1354.70, η_{cycle} = 18.46, $\eta_{Ex,HTF-ORC}$ = 26.63, η_{Ex-PI} = 6.51)								
1	64.79	1.00023	444.68	3500000	300.15	20	0.89996	0.9
w = 0.30:0.10:0.40:0.20: (Power = 1452.65, η_{cycle} = 18.44, $\eta_{Ex,HTF-ORC}$ = 26.21, η_{Ex-PI} = 6.88)								
1	74.21	1.00023	444.68	3500000	300.15	20	0.9	0.9
Single objective ($\eta_{Ex,HTF-ORC}$): (Power = 276.30, η_{cycle} = 18.42, $\eta_{Ex,HTF-ORC}$ = 29.32, η_{Ex-PI} = 3.35)								
2	40.00	0.38718	444.68	3500000	300.15	20	0.9	0.9
Single objective ($\eta_{Ex,PI}$): (Power = 634.41, η_{cycle} = 18.46, $\eta_{Ex,HTF-ORC}$ = 26.14, η_{Ex-PI} = 6.96)								
1	75.00	0.55177	444.68	3500000	300.15	5	0.9	0.9

The coconut shell fuel consistently had favorable performance in all the weighting cases. For the equal weights (0.25:0.25:0.25:0.25), the system produced approximately net 1460.54 kW of power, with a cycle efficiency of 18.44%, an HTF–ORC exergy efficiency of 26.19%, and a plant exergy efficiency of 6.90%. A weight (0.10:0.40:0.40:0.10) shift to favor HTF–ORC exergy performance produced a slightly lower power output (1354.70 kW) and in return improved the HTF–ORC exergy efficiency (26.63%). The remaining weighting patterns did not differ significantly in performance, indicating stability and robustness in these results. For comparison, single-objective optimization of the HTF–ORC exergy efficiency and the plant exergy efficiency achieved results of 29.32% and 26.14%, respectively. As expected with a focus on exergy generation, the benefits to performance came at the sacrifice of power output, which is consistent with the trade-offs demonstrated in the Pareto optimization presented.

These weights represent different design priorities for the four competing objectives, power output, cycle efficiency, and exergy efficiencies of the HTF–ORC and the overall biomass plant. Across all cases, the coconut shell fuel consistently delivered superior performance. Under equal weighting, the system produced about 1460.54 W net power with a cycle efficiency of 18.43%, HTF–ORC exergy efficiency of 26.19%, and plant exergy efficiency of 6.90%. When more weight was assigned to exergy performance (e.g., 0.10:0.40:0.40:0.10), the model favored slightly lower power (1354.70 W), but improved HTF–ORC exergy efficiency (26.63%).

For different power targets, 60 ± 2%, 120 ± 2%, 180 ± 2%, and 240 ± 2% kW, the results show clear consistency in the operating conditions as indicated in Table 5. Each power range served as a constraint, while the remaining three output features, cycle efficiency, HTF–ORC exergy efficiency, and overall biomass plant exergy efficiency, were equally weighted (1/3 each) in the evaluation. The turbine inlet temperature, upper cycle pressure, and lower cycle temperature remained close to their upper bounds across all cases, indicating that these extremes are most favorable for enhancing both thermal and exergy efficiencies of the system. This trend reinforces the effectiveness of the deep learning-based optimization in capturing the underlying thermodynamic behavior of the ORC.

Table 5. TOPSIS ranking of the Pareto optimal solutions for some output power targets.

Fuel	Mx-Str, λ	$\dot{m}_{fuel}$	T_1	P_6	T_2	ppt	η_{P}	η_{T}
Target = 60 ± 2% (Power = 61.20, η_{cycle} = 18.50, $\eta_{\text{Ex,HTF–ORC}}$ = 28.53, $\eta_{\text{Ex-Pl}}$ = 4.57)								
1	42.83	0.05000	444.68	3500000	300.15	20	0.9	0.9
Target = 120 ± 2% (Power = 121.39, η_{cycle} = 18.47, $\eta_{\text{Ex,HTF–ORC}}$ = 26.25, $\eta_{\text{Ex-Pl}}$ = 6.84)								
1	72.28	0.08670	444.68	3500000	300.15	19.31	0.89979	0.9
Target = 180 ± 2% (Power = 182.28, η_{cycle} = 18.46, $\eta_{\text{Ex,HTF–ORC}}$ = 26.13, $\eta_{\text{Ex-Pl}}$ = 6.95)								
1	75.00	0.14776	444.68	3500000	300.15	20	0.9	0.9
Target = 240 ± 2% (Power = 240.98, η_{cycle} = 18.46, $\eta_{\text{Ex,HTF–ORC}}$ = 26.13, $\eta_{\text{Ex-Pl}}$ = 6.96)								
1	74.21	1.00023	444.68	3500000	300.15	20	0.9	0.9

4. Conclusions

This study effectively created a combined deep learning-based framework to predict the performance and optimize performance parameters of a biomass-driven ORC system. The model combines detailed thermodynamic modeling based on a DNN with PSO and TOPSIS to effectively model complex trade-offs across four thermodynamic performance indicators, which are the net power, cycle efficiency, HTF–ORC exergy efficiency, and the overall biomass power plant exergy efficiency. The analysis showed that, in general, the optimal conditions occurred in the upper limits of the operational range: turbine inlet temperatures of approximately 444.68 K, pressures close to 3.5 MPa with lower cycle temperatures of 300.15 K; these improved the exergy utilization and overall efficiency. The optimum fuel was coconut shells, producing a maximum of up to 1460 kW of power with cycle efficiency of 18.44% and an HTF–ORC exergy efficiency of around 26.19%. The analysis confirmed that the preferred conditions typically occurred at the high-end of the defined operating ranges (turbine inlet temperature at 444.68 K, pressures at close to 3.5 MPa, and low cycle temperature of 300.15 K), conducive to improved exergy utilization and overall efficiency. Coconut shell was the best fuel to be researched, producing as much as 1460 kW of power with a cycle efficiency of 18.44% and an exergy efficiency for the HTF–ORC of about 26.19%. Mixture strength and biomass flowrate were evidently proportional to power target levels, confirming both the internal consistency of the optimization and the accuracy in predicting what would happen according to real thermodynamic behavior. Hence, the DNN-PSO-TOPSIS methodology has been proven to perform in a practical context for predictive and optimization ability for multi-objective biomass ORC modeling and testing. It establishes a useful data-backed design tool for future work on improvements and various applications of renewable energy generation systems, especially for decentralized and off-grid applications. Future work will extend the methodology to include validation and in-field possibilities for deployment and real-time adaptive control.

Use of AI tools declaration

The authors declare they have not used Artificial Intelligence (AI) tools in the creation of this article.

Conflict of interest

The authors declare no conflicts of interest.

Author contributions

M. O. Petinrin: Conceptualization, Data curation, Methodology, Formal analysis, Writing—original draft, Writing—review & editing, Supervision, Validation. E. D. Otolorin: Methodology, Formal analysis, Software, Validation, Visualization, Writing—original draft. O. A. Towoju: Formal analysis, Data curation, Methodology, Writing—review & editing. P. M. Singh: Formal analysis, Data curation, Visualization, Writing—review & editing.

References

1. Amjith LR, Bavanish B (2022) A review on biomass and wind as renewable energy for sustainable environment. *Chemosphere* 293: 133579. https://doi.org/10.1016/j.chemosphere.2022.133579
2. Longo S, Cellura M, Guarino F, et al. (2015) Embodied energy and environmental impacts of a biomass boiler: A life cycle approach. *AIMS Energy* 3: 214–226. https://doi.org/10.3934/energy.2015.2.214
3. Saleem M (2022) Possibility of utilizing agriculture biomass as a renewable and sustainable future energy source. *Heliyon* 8: e08905. https://doi.org/10.1016/j.heliyon. 2022.e08905
4. Kong R, Deethayat T, Asanakham A, et al. (2022) Performance analysis of biomass boiler-organic Rankine cycle with assisted cascade heat pump for combined heat and power generation including exergy-costing. *Sustainable Energy Technol Assess* 52: 102125. https://doi.org/10.1016/j.seta.2022.102125

5. Ren J, Xu C, Qian Z, et al. (2024) Exergoeconomic analysis and optimization of a biomass integrated gasification combined cycle based on externally fired gas turbine, steam Rankine cycle, organic Rankine cycle, and absorption refrigeration cycle. *Entropy* 26: 511. https://doi.org/10.3390/e26060511
6. Ang TZ, Salem M, Kamarol M, et al. (2022) A comprehensive study of renewable energy sources: Classifications, challenges and suggestions. *Energy Strategy Rev* 43: 100939. https://doi.org/10.1016/j.esr.2022.100939
7. Alvi JZ, Guan Z, Imran M (2024) Thermoeconomic evaluation and sustainability insights of hybrid solar–biomass powered organic Rankine cycle systems: A comprehensive review. *Biomass* 4: 1092–1121. https://doi.org/10.3390/biomass4040061
8. Budovich LS (2024) Energy, exergy analysis in a hybrid power and hydrogen production system using biomass and organic Rankine cycle. *Int J Thermofluids* 21: 100584. https://doi.org/10.1016/j.ijft.2024.100584
9. Yunusa SU, Mensah E, Preko K, et al. (2023) Biomass cookstoves: A review of technical aspects and recent advances. *Energy Nexus* 11: 100225. https://doi.org/10.1016/j.nexus.2023.100225
10. Antar M, Lyu D, Nazari M, et al. (2021) Biomass for a sustainable bioeconomy: An overview of world biomass production and utilization. *Renewable Sustainable Energy Rev* 139: 110691. https://doi.org/10.1016/j.rser.2020.110691
11. Kavathia K, Prajapati P (2021) A review on biomass-fired CHP system using fruit and vegetable waste with regenerative organic Rankine cycle (RORC). *Mater Today Proc* 43: 572–578. https://doi.org/10.1016/j.matpr.2020.12.052
12. Tshikovhi A, Motaung TE (2023) Technologies and innovations for biomass energy production. *Sustainability* 15: 12121. https://doi.org/10.3390/su151612121
13. Ping X, Yang F, Zhang H, et al. (2021) Prediction and optimization of power output of single screw expander in organic Rankine cycle (ORC) for diesel engine waste heat recovery. *Appl Therm Eng* 182: 116048. https://doi.org/10.1016/j.applthermaleng.2020.116048
14. Abbas WKA, Baumhögger E, Vrabec J (2022) Experimental investigation of organic Rankine cycle performance using alkanes or hexamethyldisiloxane as a working fluid. *Energy Convers Manag X* 15: 100244. https://doi.org/10.1016/j.ecmx.2022.100244
15. Dumont O, Dickes R, De Rosa M, et al. (2018) Technical and economic optimization of subcritical, wet expansion and transcritical organic Rankine cycle (ORC) systems coupled with a biogas power plant. *Energy Convers Manag* 157: 294–306. https://doi.org/10.1016/j.enconman.2017.12.022
16. Loni R, Mahian O, Najafi G, et al. (2021) A critical review of power generation using geothermal-driven organic Rankine cycle. *Therm Sci Eng Prog* 25: 101028. https://doi.org/10.1016/j.tsep.2021.101028
17. Kumar A, Rakshit D (2021) A critical review on waste heat recovery utilization with special focus on organic Rankine cycle applications. *Clean Eng Technol* 5: 100292. https://doi.org/10.1016/j.clet.2021.100292
18. Xu W, Zhang J, Zhao L, et al. (2017) Novel experimental research on the compression process in organic Rankine cycle (ORC). *Energy Convers Manag* 137: 1–11. https://doi.org/10.1016/j.enconman.2017.01.025

19. Salem M, Alavi MF, Mahariq I, et al. (2021) Applications of thermal energy storage in solar organic Rankine cycles: A comprehensive review. *Front Energy Res* 9: 1–11. https://doi.org/10.3389/fenrg.2021.766292
20. Heidarnejad P, Genceli H, Hashemian N, et al. (2024) Biomass-fueled organic Rankine cycles: State of the art and future trends. *Energies* 17: 3788. https://doi.org/10.3390/en17153788
21. Liu H, Qiu G, Shao Y, et al. (2010) Preliminary experimental investigations of a biomass-fired micro-scale CHP with organic Rankine cycle. *Int J Low-Carbon Technol* 5: 81–87. https://doi.org/10.1093/ijlct/ctq005
22. Zhao D, Deng S, Zhao L, et al. (2020) Energy and AI overview on artificial intelligence in design of organic Rankine cycle. *Energy AI* 1: 100011. https://doi.org/10.1016/j.egyai.2020.100011
23. López-flores FJ, Rubio-castro E, Ponce-Ortega JM (2022) Incorporating machine learning for thermal engines modeling in industrial waste heat recovery. *Chem Eng Res Des* 181: 239–252. https://doi.org/10.1016/j.cherd.2022.03.022
24. Ping X, Yang F, Zhang H, et al. (2022) Evaluation of hybrid forecasting methods for organic Rankine cycle : Unsupervised learning-based outlier removal and partial mutual information-based feature selection. *Appl Energy* 311: 118682. https://doi.org/10.1016/j.apenergy.2022.118682
25. Oyekale J, Oreko B (2023) Machine learning for design and optimization of organic Rankine cycle plants : A review of current status and future perspectives. *WIREs Energy Environ* 1–18. https://doi.org/10.1002/wene.474
26. Li X, Zhong K, Feng L (2023) Machine learning-based metaheuristic optimization of an integrated biomass gasification cycle for fuel and cooling production. *Fuel* 332: 125969. https://doi.org/10.1016/j.fuel.2022.125969
27. Okoroafor RE, Smith CM, Ochie IK, et al. (2022) Geothermics machine learning in subsurface geothermal energy : Two decades in review. *Geothermics* 102: 102401. https://doi.org/10.1016/j.geothermics.2022.102401
28. Daniarta S, Kolasinski P, Imre AR, et al. (2024) Artificial intelligence-driven performance mapping: A deep learning-based investigation of a multi-vane expander in retrofitted organic Rankine cycle. *Energy Convers Manag* 315: 1–27. https://doi.org/10.1016/j.enconman.2024.118763
29. Mert İ, Bilgic HH, Yağli H, et al. (2020) Deep neural network approach to estimation of power production for an organic Rankine cycle system. *J Braz Soc Mech Sci Eng* 42. https://doi.org/10.1007/s40430-020-02701-y
30. van Giffen B, Herhausen D, Fahse T (2022) Overcoming the pitfalls and perils of algorithms: A classification of machine learning biases and mitigation methods. *J Bus Res* 144: 93–106. https://doi.org/10.1016/j.jbusres.2022.01.076
31. Flores-Tlacuahuac A, Gutierrez-Limon MA, Sales-Cruz M (2022) A probabilistic deep learning approach for thermal and exergy forecasting in organic Rankine cycles. *Comput Chem Eng* 168: 108029. https://doi.org/10.1016/j.compchemeng.2022.108029
32. Kim JS, Kim DY, Kim YT (2019) Experiment on radial inflow turbines and performance prediction using deep neural network for the organic Rankine cycle. *Appl Therm Eng* 149: 633–643. https://doi.org/10.1016/j.applthermaleng.2018.12.084

33. Molina NAD, Olivier JAS, Canepa JRL, et al. (2024) Evaluation of the bioenergy potential of agricultural and agroindustrial waste generated in southeastern Mexico. *AIMS Energy* 12: 984–1009. https://doi.org/10.3934/energy.2024046
34. Ozyuguran A, Akturk A, Yaman S (2018) Optimal use of condensed parameters of ultimate analysis to predict the calorific value of biomass. *Fuel* 214: 640–646. https://doi.org/10.1016/j.fuel.2017.10.082
35. Basu P (2013) *Biomass Gasification, Pyrolysis and Torrefaction: Practical Design and Theory*. 2nd Edition, Elsevier, San Diego. https://doi.org/10.1016/C2011-0-07564-6
36. Jacob RC, Pannir S, Abdalla ME (2022) Energy analysis of biomass integrated air gasification regenerative gas turbine power plants, *International Refrigeration and Air Conditioning Conference*. Available from: https://docs.lib.purdue.edu/iracc/2274/.
37. Effatpanah SK, Ahmadi MH, Delbari SH, et al. (2022) Energy, exergy, exergoeconomic and emergy—based exergoeconomic (emergoeconomic) analyses of a biomass combustion waste heat recovery organic Rankine cycle. *Entropy* 24: 209. https://doi.org/10.3390/e24020209
38. Solutia (2025) Therminol VP-1: Heat Transfer Fluid. *Technical Bulletin 72391158*. Available from: https://www.sintelub.com/wp-content/uploads/PDS/37.therminol_vp1.pdf.
39. Bull J, Pound J, Radulovic J, et al. (2025) Low-temperature ORC systems: Influence of the Approach point and pinch point temperature differences. *Energies* 18: 2954. https://doi.org/10.3390/en18112954
40. Li C, Wang H (2016) Power cycles for waste heat recovery from medium to high temperature flue gas sources—From a view of thermodynamic optimization. *Appl Energy* 180: 707–721. https://doi.org/10.1016/j.apenergy.2016.08.007
41. Fu BR, Hsu SW, Lee YR, et al. (2014) Performance of a 250 kW organic Rankine cycle system for off-design heat source conditions. *Energies* 7: 3684–3694. https://doi.org/10.3390/en7063684
42. Kezrane C, Laouid YA, Lasbet Y, et al. (2018) Comparison of different organic Rankine cycle for power generation using waste heat. *Eur J Electr Eng* 20: 151–169. https://doi.org/10.3166/EJEE.20.151-169
43. Yari M (2010) Exergetic analysis of various types of geothermal power plants. *Renewable Energy* 35: 112–121. https://doi.org/10.1016/j.renene.2009.07.023
44. Ahmadi P, Dincer I (2011) Thermodynamic and exergoenvironmental analyses, and multi-objective optimization of a gas turbine power plant. *Appl Therm Eng* 31: 2529–2540. https://doi.org/10.1016/j.applthermaleng.2011.04.018
45. Ahmadi P, Dincer I (2011) Thermodynamic analysis and thermoeconomic optimization of a dual pressure combined cycle power plant with a supplementary firing unit. *Energy Convers Manag* 52: 2296–2308. https://doi.org/10.1016/j.enconman.2010.12.023
46. Ahmadi P, Dincer I, Rosen MA (2011) Exergy, exergoeconomic and environmental analyses and evolutionary algorithm based multi-objective optimization of combined cycle power plants. *Energy* 36: 5886–5898. https://doi.org/10.1016/j.energy.2011.08.034
47. Elmaihy A, Rashad A, Elweteedy A, et al. (2023) Energy and exergy analyses for organic Rankine cycle driven by cooling water of passenger car engine using sixteen working fluids. *Energy Convers Manag X* 20: 100415. https://doi.org/10.1016/j.ecmx.2023.100415
48. Song G, Shen L, Xiao J (2011) Estimating specific chemical exergy of biomass from basic analysis data. *Ind Eng Chem Res* 50: 9758–9766. https://doi.org/10.1021/ie200534n

49. Dubey SR, Singh SK, Chaudhuri BB (2022) Activation functions in deep learning: A comprehensive survey and benchmark. *Neurocomputing* 503: 92–108. https://doi.org/10.1016/j.neucom.2022.06.111
50. Kılıçarslan S, Adem K, Çelik M (2021) An overview of the activation functions used in deep learning algorithms. *J New Results Sci* 10: 75–88. https://doi.org/10.54187/jnrs.1011739
51. Ioffe S, Szegedy C (2015) Batch normalization: Accelerating deep network training by reducing internal covariate shift, *Proceedings of the 32nd International Conference on Machine Learning,* PMLR, 37: 448–456. Available from: https://proceedings.mlr.press/v37/ioffe15.html.
52. Kingma DP, Ba JL (2015) Adam: A method for stochastic optimization. Preprint. https://doi.org/10.48550/arXiv.1412.6980
53. Zhang J, Hu F, Li L, et al. (2018) An adaptive mechanism to achieve learning rate dynamically. *Neural Comput Appl* 31: 6685–6698. https://doi.org/10.1007/s00521-018-3495-0
54. You K, Long M, Wang J, et al. (2019) How does learning rate decay help modern neural networks? Preprint. https://doi.org/10.48550/arXiv.1908.01878
55. Feng YQ, Zhang Q, Xu KJ, et al. (2023) Operation characteristics and performance prediction of a 3 kW organic Rankine cycle (ORC) with automatic control system based on machine learning methodology. *Energy* 263: 125857. https://doi.org/10.1016/j.energy.2022.125857
56. Olatunji OO, Akinlabi S, Madushele N, et al. (2019) Multilayer perceptron artificial neural network for the prediction of heating value of municipal solid waste. *AIMS Energy* 7: 944–956. https://doi.org/10.3934/energy.2019.6.944
57. Peng Y, Lin X, Liu J, et al. (2021) Machine learning prediction of ORC performance based on properties of working fluid. *Appl Therm Eng* 195: 117184. https://doi.org/10.1016/j.applthermaleng.2021.117184
58. Wang W, Deng S, Zhao D, et al. (2020) Application of machine learning into organic Rankine cycle for prediction and optimization of thermal and exergy efficiency. *Energy Convers Manag* 210: 112700. https://doi.org/10.1016/j.enconman.2020.112700
59. Wang HX, Lei B, Cao JY, et al. (2025) Multi-objective optimization of a multiple heat sources small-scale organic Rankine cycle with quasi two stage single screw expander using machine learning techniques. *Energy* 339: 139083. https://doi.org/10.1016/j.energy.2025.139083
60. Wang Z, Yi Q, Zhao Y, et al. (2025) Parameter analysis and multi-objective optimization of organic Rankine cycle coupled vapor compression cycle using PSO-BPNN model. *Appl Therm Eng* 273: 126583. https://doi.org/10.1016/j.applthermaleng.2025.126583
61. Petinrin MO, Labiran MJ, Bello-Ochende T, et al. (2022) Thermodynamic optimization of parallel and spiral plate heat exchangers for modified solar thermal Brayton cycle models. *Sci Afr* 16: e01262. https://doi.org/10.1016/j.sciaf.2022.e01262
62. Wang L, Hong L, Fu H, et al. (2025) Adaptive distance-based multi-objective particle swarm optimization algorithm with simple position update. *Swarm Evol Comput* 94: 101890. https://doi.org/10.1016/j.swevo.2025.101890
63. Ping X, Yang F, Zhang H, et al. (2023) Ensemble learning-based nonlinear time series prediction and dynamic multi-objective optimization of organic Rankine cycle (ORC) under actual driving cycle. *Eng Appl Artif Intell* 126: 106979. https://doi.org/10.1016/j.engappai.2023.106979
64. Xing C, Ping X, Guo R, et al. (2023) Machine learning-based multi-objective optimization and thermodynamic evaluation of organic Rankine cycle (ORC) system for vehicle engine under road condition. *Appl Therm Eng* 231: 120904. https://doi.org/10.1016/j.applthermaleng.2023.120904

65. Chakraborty S (2022) TOPSIS and modified TOPSIS: A comparative analysis. *Decis Anal J* 2: 100021. https://doi.org/10.1016/j.dajour.2021.100021
66. Ciardiello F, Genovese A (2023) A comparison between TOPSIS and SAW methods. *Ann Oper Res* 325: 967–994. https://doi.org/10.1007/s10479-023-05339-w
67. Wang Y, Liu P, Yao Y (2022) BMW-TOPSIS: A generalized TOPSIS model based on three-way decision. *Inf Sci* 607: 799–818. https://doi.org/10.1016/j.ins.2022.06.018
68. El-Hashash EF, Shiekh RHA (2022) A comparison of the Pearson, Spearman Rank and Kendall Tau correlation coefficients using quantitative variables. *Asian J Probab Stat* 20: 36–48. https://doi.org/10.9734/ajpas/2022/v20i3425
69. Zhang L, Wang L (2023) Optimization of site investigation program for reliability assessment of undrained slope using Spearman rank correlation coefficient. *Comput Geotech* 155: 105208. https://doi.org/10.1016/j.compgeo.2022.105208
70. Colquhoun D (2014) An investigation of the false discovery rate and the misinterpretation of p-values. *R Soc Open Sci* 1: 140216. https://doi.org/10.1098/rsos.140216
71. Kim K, Lee H, Kang M, et al. (2022) A machine learning approach for predicting heat transfer characteristics in micro-pin fin heat sinks. *Int J Heat Mass Transfer* 194. https://doi.org/10.1016/j.ijheatmasstransfer.2022.123087
72. Cantera (2025) Calculating Heating Value of a Fuel, *Cantera Developers*. Available from: https://cantera.org/dev/userguide/heating-value.html.
73. Cantera (2025) Calculating Adiabatic Flame Temperature, *Cantera Developers*. Available from: https://cantera.org/dev/userguide/flame-temperature.html.
74. Marzouk OA (2023) Adiabatic flame temperatures for oxy-methane, oxy-hydrogen, air-methane, and air-hydrogen stoichiometric combustion using the NASA CEARUN tool, GRI-Mech 3.0 reaction mechanism, and Cantera Python package. *Eng Technol Appl Sci Res* 13: 11437–11444. https://doi.org/10.48084/etasr.6132
75. Mariani A, Mastellone ML, Morrone B, et al. (2020) An organic Rankine cycle bottoming a diesel engine powered passenger car. *Energies* 13: 1–16. https://doi.org/10.3390/en13020314